J. Mech. Phys. Solids 148 (2021) 104292

Contents lists available at ScienceDirect

Journal of the Mechanics and Physics of Solids

journal homepage: www.elsevier.com/locate/jmps

Modeling actuation and sensing in ionic polymer metal composites by electrochemo-poromechanics

Alessandro Leronni, Lorenzo Bardella *

Department of Civil, Environmental, Architectural Engineering and Mathematics (DICATAM), University of Brescia, Via Branze, 43 25123, Brescia, Italy

ARTICLE INFO

Keywords:
Ionic polymer metal composite
Sensors and actuators
Porous material
Chemo-mechanical processes
Electromechanical processes

ABSTRACT

Ionic polymer metal composites (IPMCs) consist of an electroactive polymeric membrane plated with metal electrodes. They hold promise as actuators and sensors for soft robotics and biomedical applications. Their capabilities ensue from the motion, within the membrane, of a fluid phase consisting of ions dispersed in a solvent. Toward a thorough understanding of IPMC multiphysics, we propose a large deformation theory combining electrochemistry and poromechanics. Namely, we modify the theory recently developed by Porfiri's group by introducing the transport of the solvent, whose redistribution determines the volumetric deformation of the fluid-saturated membrane, and we further account for the cross-diffusion of solvent and ions. In actuation, the imposed voltage drop across the electrodes triggers ion migration, such that the solvent is transported toward the cathode by electro-osmosis. This determines the initial bending toward the anode; then, back-relaxation occurs because of both the solvent counter-diffusion and the asymmetric redistribution of ions near the electrodes. In short-circuit sensing, the applied load triggers solvent motion, such that ions are mainly transported toward the cathode by convection with the solvent. This determines charge accumulation; then, ion counter-diffusion leads to a decrease of the charge stored at the electrodes. We demonstrate that these behaviors can be predicted by the proposed theory on the basis of relevant finite element benchmarks. Additionally, our analysis encompasses the assessment of the role of the membrane elastic moduli in the counter-diffusion of solvent and ions in IPMC actuation and sensing.

1. Introduction

Ionic polymer metal composites (IPMCs) are micron-scale layered devices (Shahinpoor and Kim, 2001) whose core, denoted as the *membrane*, consists of a negatively charged polymer soaked in a fluid phase constituted by a solvent and positively charged mobile ions, referred to as *counterions*. The membrane is plated with thin metal sheets, assuming the roles of electrodes and sandwich skins for the electrical and mechanical behaviors, respectively. Belonging to the broader category of ionic electroactive polymers, IPMCs can potentially find application as actuators and sensors for soft robotics and biomedicine (Shahinpoor and Kim, 2005; Pugal et al., 2010; Jo et al., 2013), also fostered by recent advancements in their manufacturing (Carrico et al., 2015).

IPMCs are characterized by an inherently complex response, resulting from the nonlinear interplay among electrostatics, ion and solvent transport, and mechanics. Since the pioneering contributions of Nemat-Nasser and Li (2000) and Shahinpoor and Kim (2004), several models have been proposed for actuation and sensing of IPMCs. Our contribution builds on the thermodynamically consistent

* Corresponding author.
E-mail addresses: a.leronni@unibs.it (A. Leronni), lorenzo.bardella@ing.unibs.it (L. Bardella).

https://doi.org/10.1016/j.jmps.2021.104292
Received 3 August 2020; Received in revised form 23 November 2020; Accepted 1 January 2021
Available online 5 January 2021
0022-5096/

electrochemomechanical theory recently developed by Cha and Porfiri (2014). This finite deformation theory is inspired by previous efforts of Hong et al. (2010) on polyelectrolyte gels and encompasses mechanical, mixing, and polarization contributions to the free energy density stored within the membrane. In particular, the mixing free energy of counterions and polymer chains is written in terms of counterion concentration and volume ratio. First, this results into an osmotic stress that, along with the Maxwell stress, plays the role of an active stress (or eigenstress), to be balanced by the mechanical stress, the latter being associated with deformation. Second, it provides a contribution to the counterion flux that depends on the volume ratio gradient, balancing the electrodiffusive contribution at equilibrium. These two features of the theory underlie the modeling of actuation and sensing, respectively.

On the basis of this theory, several studies have been later conducted. Volpini et al. (2017) and Volpini and Bardella (2021) have focused on modeling the short-circuit sensing response elicited by through-the-thickness compression. Porfiri et al. (2017, 2018) have proposed an alternative explanation of the *back-relaxation* phenomenon in actuation, based on the competition between osmotic and Maxwell stresses. Recent works have revealed the importance of considering complex deformation states, with the consequent need for sophisticated structural theories if, toward efficient design and optimization, one wants to avoid cumbersome numerical models of IPMCs treated as continua (Leronni and Bardella, 2019; Boldini and Porfiri, 2020; Boldini et al., 2020).

As many other theories in the literature, the Cha and Porfiri (2014) framework disregards the solvent transport within the membrane, assuming that the IPMC electroactive properties are exclusively established by the counterion motion (Farinholt and Leo, 2004; Branco and Dente, 2006; Chen et al., 2007; Pugal et al., 2011; Nardinocchi et al., 2011). However, a few works highlight the importance of modeling the solvent dynamics, contributing to explain the back-relaxation (Shahinpoor and Kim, 2004; Schicker and Wallmersperger, 2013; Zhu et al., 2013).

Here, we develop a theory for IPMCs that combines relevant features from the Cha and Porfiri (2014) theory, the mixture theory (Bowen, 1980; Ateshian, 2007; Bluhm et al., 2016), and the recently developed theories for polyelectrolyte gels (Hong et al., 2010; Zhang et al., 2020). Specifically, we describe the membrane as a mixture of a charged polymer and a fluid phase consisting of solvent and counterions, all coexisting within each *macroscopic* point in our continuum formulation. Moreover, each constituent is assumed to be intrinsically (that is, at the *microscopic* scale) incompressible, such that the volumetric deformation of the membrane depends on the flow of the fluid phase only.

The model relies on four balance equations, written with respect to the reference configuration, which is undeformed and electroneutral: the *overall* momentum balance, two individual mass balances for solvent and counterions, and the Gauss law. The free energy density is assumed to consist of three contributions, namely accounting for the stretching of the polymer chains (*macroscopically* resulting in compressible hyperelasticity of the membrane), the mixing of solvent and counterions, and the dielectric polarization of the membrane. The dissipation is due to the fluxes of solvent and counterions, in which, noticeably, we also account for their *cross-diffusion*, whereby the flux of each species is governed by the (electro)chemical potential gradients of both species (Vanag and Epstein, 2009; Zhu et al., 2013; Zhang et al., 2020).

Aiming at providing the essential multiphysical framework, including solvent transport, to thoroughly explain IPMC actuation and sensing, we assume that the fluid phase is a dilute and ideal solution, and we neglect both entropic and energetic interactions between the fluid phase and the polymeric solid phase. That is, we assume that the IPMC membrane is an *ideal* mixture (Ateshian, 2007).

Our effort results in a theory coupling electrochemistry and poromechanics of IPMCs. Specifically, the electrochemistry describes the distribution of counterions within the membrane and the related electric potential field; it is governed by a Poisson–Nernst–Planck system of equations, which ensues from the mass balance for the counterions and the Gauss law, and results to be modified, with respect to its classical version (Porfiri, 2008), by both the addition of the convective flux of counterions with the solvent and the background membrane deformation. The poromechanics describes the overall deformation field of the membrane by accounting for the solvent flow in the porous network; with respect to classical poromechanics (Coussy, 2004; MacMinn et al., 2016), both the electro-osmotic flux of the solvent and the Maxwell stress enter the governing equations, which rely on the overall momentum balance and the mass balance for the solvent.

Previous efforts on IPMCs have already resorted to the theories of mixtures and porous media, although by either limiting the theoretical development or disregarding relevant phenomena to more easily focus on specific aspects of the IPMC behavior. For instance, Del Bufalo et al. (2008) and Tixier and Pouget (2020) have applied their mixture theory-based models to analyze the steady state actuation of IPMCs regarded as Euler–Bernoulli beams, under small and large strains, respectively. By taking advantage of the theory of porous media, Leichsenring et al. (2017) have derived a model neglecting both solvent flux and membrane deformation to study the influence of the solvent volume fraction on IPMC electrochemistry.

Here, we apply our proposal to a continuum IPMC cantilever strip subjected either to a fixed voltage across the electrodes (actuation problem) or to a uniformly distributed load under short-circuit condition (sensing problem). We solve these problems by resorting to the commercial finite element code *COMSOL Multiphysics®*. In actuation, as an original contribution of this work, we predict and explain the back-relaxation phenomenon (Asaka et al., 1995) in terms of the interplay between the *solvent counter-diffusion* (Shahinpoor and Kim, 2004) and the asymmetric growth of the Maxwell stress near the electrodes (Porfiri et al., 2017). Dually, in sensing, our theory can anticipate the discharge under a sustained mechanical stimulus (Farinholt and Leo, 2004) and explain it in terms of the *counterion counter-diffusion*. We demonstrate how these behaviors are influenced by the membrane elastic moduli entering the selected hyperelastic strain energy density, where volumetric and deviatoric deformations are coupled.

2. An electrochemo-poromechanical theory for IPMCs

2.1. Fundamental kinematics-related assumptions

We assume that the IPMC membrane consists of a solid phase identifying with a charged polymer and of a fluid phase represented by an uncharged solvent in which counterions are immersed. Analogously to mixture theory, all the phases coexist within each single material point (Ateshian, 2007). By definition, the deformation gradient, written in terms of the displacement vector $\mathbf{u}$, reads

$$\mathbf{F} = \mathbf{I} + \nabla\mathbf{u} \tag{1}$$

and describes the motion of a material point from the reference (initial) configuration, which is undeformed and electroneutral (Cha and Porfiri, 2014), to the current configuration.[1]

Importantly, the solvent always saturates the membrane. This aspect distinguishes our model from most on the swelling of polymeric gels, which identify the reference configuration with the space region occupied by the dry polymer (Hong et al., 2008; Chester and Anand, 2010).

Throughout the manuscript, we refer to *nominal* molar concentrations, that is, molar concentrations per unit *reference total* volume. Alternatively, in the literature, molar concentrations are often expressed per unit volume of the fluid phase only (Ateshian, 2007). Noticeably, in this first investigation on the IPMC electrochemo-poromechanics, we assume that the solution of solvent and counterions is *dilute*, that is,

$$C \ll C_{\mathrm{s}}\,, \tag{2}$$

where C and C_{s} are the nominal molar concentrations of counterions and solvent, respectively. This is convenient in the light of the challenging computational models ensuing from such multiphysical theories, even when neglecting the solvent transport (Boldini and Porfiri, 2020; Boldini et al., 2020). Accordingly (Ateshian, 2007), we neglect the volume occupied by counterions and hypothesize that both solvent molecules and polymer chains are intrinsically incompressible, which is a common practice for polyelectrolyte gels as well (Zhang et al., 2020). Therefore, volumetric deformations are inextricably related to variations of the solvent concentration only, such that the following kinematic constraint holds:

$$J \equiv \det\mathbf{F} = 1 + \upsilon_{\mathrm{s}}\left(C_{\mathrm{s}} - C_{\mathrm{s}}^{0}\right)\,, \tag{3}$$

whose rate form is

$$\underbrace{J\mathbf{F}^{-\mathrm{T}}\cdot\dot{\mathbf{F}}}_{\dot{J}} - \upsilon_{\mathrm{s}}\dot{C}_{\mathrm{s}} = 0\,. \tag{4}$$

Here and henceforth, J is the volume ratio, υ_{s} is the solvent molar volume, and C_{s}^{0} is the initial value of C_{s}. Moreover, the symbol $\cdot$ denotes the inner product and $\dot{}$ indicates partial time derivative, such that $\dot{C}_{\mathrm{s}}(\mathbf{X},t) \equiv \partial C_{\mathrm{s}}(\mathbf{X},t)/\partial t$, with t representing time.

We anticipate that we assume a purely elastic $\mathbf{F}$. Hence, the allowed volumetric deformation due to solvent transport will require the selection of a *compressible* hyperelastic strain energy, as for instance proposed by Hong et al. (2010) for polyelectrolyte gels. We observe that the elastic deformation could be constrained to be isochoric by adopting a richer kinematics in which $\mathbf{F}$ would involve inelastic contributions, such as the swelling term in the theory of Chester and Anand (2010) for polymeric gels.

2.2. Balance equations

The present model relies on four balance equations, written in the reference configuration: the overall momentum balance (that is, the momentum balance for the mixture as a whole), the mass balances for the solvent and counterions, and the Gauss law.

We assume that mechanical equilibrium is rapidly attained in comparison to the time scale characterizing the fluid phase transport (Hong et al., 2010; Cha and Porfiri, 2014). Hence, by neglecting inertial effects, the overall momentum balance in the absence of body forces reads

$$\mathrm{Div}\,\mathbf{P} = \mathbf{0}\,, \tag{5}$$

where Div is the material divergence and $\mathbf{P}$ is the nominal stress tensor, such that $(\mathrm{Div}\,\mathbf{P})_i = \partial P_{iJ}/\partial X_J$.[2]

The mass balance for the solvent reads

$$\dot{C}_{\mathrm{s}} + \mathrm{Div}\,\mathbf{J}_{\mathrm{s}} = 0\,, \tag{6}$$

in which $\mathbf{J}_{\mathrm{s}}$ is the nominal molar solvent flux, that is, the molar flux per unit reference total area.

[1] In Eq. (1), $\mathbf{I}$ is the second order identity tensor and the symbol ∇ denotes the material gradient, such that $(\nabla\mathbf{u})_{iJ} = \partial u_i/\partial X_J$, in which $\mathbf{X}$ is the material position vector and small case and capital case subscripts indicate the spatial and material coordinates, respectively.

[2] Although here, by following Hong et al. (2010), $\mathbf{P}$ is referred to as the *nominal* stress tensor, for the sake of clarity, we note that in the literature it is also denoted as the first Piola–Kirchhoff stress tensor (Ogden, 1984).

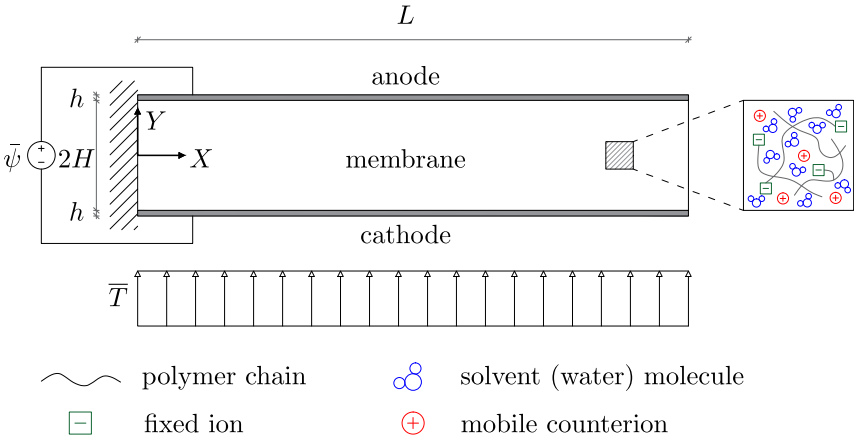

Fig. 1. Cantilever IPMC subjected to an applied voltage $\bar{\psi}$ across the electrodes (non-zero in the actuation problem) and to an imposed nominal surface load $\overline{T}$ (non-zero in the sensing problem): geometrical parameters, reference system, and physical constituents.

Analogously, the mass balance for the counterions is

$$\dot{C} + \mathrm{Div}\,\mathbf{J} = 0\,,$$

with $\mathbf{J}$ denoting the nominal molar counterion flux.

The Gauss law reads

$$\mathrm{Div}\,\mathbf{D} = F(C - C^0)\,, \tag{7}$$

where $\mathbf{D}$ is the nominal electric displacement, F is the Faraday constant, and C^0 is the nominal molar concentration of the anions fixed to the polymer. In Eq. (7), we assume that both fixed anions and mobile counterions have unit valency, which is usually the case for IPMCs. These two ionic species are the only ones that contribute to IPMC electrochemistry (Shahinpoor and Kim, 2001; Porfiri, 2008).

We treat the electrodes as perfect electric conductors that are impermeable to both solvent and ions. Therefore, they establish boundary conditions for both the solvent transport and the electrochemical problems in the membrane and, of the foregoing balance laws, are subject to Eq. (5) only.

2.2.1. *Boundary and initial conditions*

With reference to Fig. 1, the IPMC has length L, membrane thickness $2H$, and *thin* electrodes of thickness h. We consider the usual case of a very slender IPMC, such that $L \gg 2(H + h)$.

About mechanics, in both the actuation and sensing problems, we consider a cantilever configuration with clamped side at the left end, such that

$$\mathbf{u} = \mathbf{0} \quad \text{at } X = 0\,.$$

The rest of the boundary is subjected to static boundary conditions. Specifically, the edges at $X = L$ and $Y = H + h$ are always stress-free, while the remaining side is either stress-free in the actuation problem or subjected to

$$\mathbf{T} \equiv \mathbf{P}\mathbf{N} = -\overline{T}\mathbf{N} \quad \text{at } Y = -H - h \tag{8}$$

in the sensing problem. In Eq. (8), $\mathbf{T}$ is the nominal traction (that is, $T_i \equiv P_{iJ}N_J$), $\mathbf{N}$ is the outward unit normal to the reference boundary, and $\overline{T}$ is the magnitude of the uniformly distributed nominal load. In the benchmark of Section 3.4, this load will be applied in a suitably short time to unveil the effect of the counter-diffusion of mobile ions.

We assume that the electrodes are impermeable to both solvent and counterions by imposing the zero-flux boundary conditions

$$\mathbf{J}_s \cdot \mathbf{N} = 0 \quad \text{and} \quad \mathbf{J} \cdot \mathbf{N} = 0 \quad \text{at } Y = \pm H\,.$$

Given the IPMC slenderness, we may disregard the edge effects at the IPMC ends, such that, in the simulations, we find it convenient to extend these boundary conditions to $X = 0$ and $X = L$.

Finally, we express the boundary conditions for the electrostatics as

$$\psi = \frac{\bar{\psi}}{2} \quad \text{at } Y = H \quad \text{and} \quad \psi = -\frac{\bar{\psi}}{2} \quad \text{at } Y = -H\,,$$

in which ψ is the electric potential and $\bar{\psi}$ is the applied voltage drop across the electrodes. Specifically, $\bar{\psi} \neq 0$ in the actuation problem, while $\bar{\psi} = 0$ in the short-circuit sensing problem. In the actuation benchmark of Section 3.3, $\bar{\psi}$ will be suddenly applied

to unveil the phenomena behind back-relaxation. At the IPMC ends $X = 0$ and $X = L$ it is convenient to prevent accumulation of surface charge by imposing $\mathbf{D} \cdot \mathbf{N} = 0$.

The mass balances also need initial conditions, which are

$$C_\mathrm{s} = C_\mathrm{s}^0 \quad \text{at } t = 0\,, \tag{9a}$$

$$C = C^0 \quad \text{at } t = 0\,. \tag{9b}$$

Eq. (9b) implies the electroneutrality of the reference configuration.

2.3. Thermodynamic restrictions

We follow the approach of Gurtin et al. (2010) for coupled problems of mechanics and species transport, augmented to take into account that counterions are electrically charged species. Given that we focus on isothermal conditions, we disregard the heat terms in the thermodynamic laws. Hence, the energy balance encompasses mechanical, electrical, and species transport contributions:

$$\dot{U} = \mathbf{P} \cdot \dot{\mathbf{F}} + \mathbf{E} \cdot \dot{\mathbf{D}} + \mu_\mathrm{s} \dot{C}_\mathrm{s} + \mu \dot{C} - \mathbf{J}_\mathrm{s} \cdot \nabla \mu_\mathrm{s} - \mathbf{J} \cdot \nabla \tilde{\mu}\,,$$

in which U is the nominal internal energy density,

$$\mathbf{E} = -\nabla \psi \tag{10}$$

is the nominal electric field, μ_s is the solvent chemical potential (with units of energy per mole), μ is the counterion chemical potential, and

$$\tilde{\mu} = \mu + F\psi \tag{11}$$

is the counterion electrochemical potential.

By introducing the nominal Helmholtz free energy density W, and by accounting for the constraint (4), the second law of thermodynamics reads

$$\left(\mathbf{P} + p_\mathrm{s} J \mathbf{F}^{-\mathrm{T}}\right) \cdot \dot{\mathbf{F}} + \mathbf{E} \cdot \dot{\mathbf{D}} + \left(\mu_\mathrm{s} - v_\mathrm{s} p_\mathrm{s}\right) \dot{C}_\mathrm{s} + \mu \dot{C} - \mathbf{J}_\mathrm{s} \cdot \nabla \mu_\mathrm{s} - \mathbf{J} \cdot \nabla \tilde{\mu} - \dot{W} \geq 0\,, \tag{12}$$

where p_s is a Lagrange multiplier (Chester and Anand, 2010; Zhang et al., 2020). We assume that W is a function of the primal variables $\mathbf{F}$, $\mathbf{D}$, C_s, and C. Hence, substituting $\dot{W}$ in Eq. (12), by chain rule, leads to

$$\left(\mathbf{P} + p_\mathrm{s} J \mathbf{F}^{-\mathrm{T}} - \frac{\partial W}{\partial \mathbf{F}}\right) \cdot \dot{\mathbf{F}} + \left(\mathbf{E} - \frac{\partial W}{\partial \mathbf{D}}\right) \cdot \dot{\mathbf{D}} + \left(\mu_\mathrm{s} - v_\mathrm{s} p_\mathrm{s} - \frac{\partial W}{\partial C_\mathrm{s}}\right) \dot{C}_\mathrm{s} + \left(\mu - \frac{\partial W}{\partial C}\right) \dot{C} - \mathbf{J}_\mathrm{s} \cdot \nabla \mu_\mathrm{s} - \mathbf{J} \cdot \nabla \tilde{\mu} \geq 0\,.$$

By resorting to the Coleman–Noll procedure, we obtain the general constitutive relations

$$\mathbf{P} = \frac{\partial W}{\partial \mathbf{F}} - p_\mathrm{s} J \mathbf{F}^{-\mathrm{T}}\,, \quad \mathbf{E} = \frac{\partial W}{\partial \mathbf{D}}\,, \quad \mu_\mathrm{s} = \frac{\partial W}{\partial C_\mathrm{s}} + v_\mathrm{s} p_\mathrm{s}\,, \quad \mu = \frac{\partial W}{\partial C}\,, \tag{13}$$

such that the dissipation inequality reduces to

$$-\mathbf{J}_\mathrm{s} \cdot \nabla \mu_\mathrm{s} - \mathbf{J} \cdot \nabla \tilde{\mu} \geq 0\,. \tag{14}$$

We assume that each flux is a linear combination of $\nabla \mu_\mathrm{s}$ and $\nabla \tilde{\mu}$, that is

$$\mathbf{J}_\mathrm{s} = -\mathbf{M}_\mathrm{ss} \nabla \mu_\mathrm{s} - \mathbf{M}_\mathrm{s} \nabla \tilde{\mu}\,, \tag{15a}$$

$$\mathbf{J} = -\mathbf{M}_\mathrm{s} \nabla \mu_\mathrm{s} - \mathbf{M} \nabla \tilde{\mu}\,, \tag{15b}$$

where the constitutive operators can be collected into a symmetric mobility matrix (Onsager, 1931)

$$\mathcal{M} = \begin{bmatrix} \mathbf{M}_\mathrm{ss} & \mathbf{M}_\mathrm{s} \\ \mathbf{M}_\mathrm{s} & \mathbf{M} \end{bmatrix} \tag{16}$$

to be defined such that Eq. (14) is fulfilled. The assumption that the flux of a species also depends on the (electro)chemical potential gradient of the other species (that is, $\mathbf{M}_\mathrm{s} \neq \mathbf{0}$) is usually referred to as *cross-diffusion* (Vanag and Epstein, 2009). The description of this phenomenon, which has been observed to be relevant for IPMCs (Zhu et al., 2013), constitutes one of the main concerns of our investigation.

2.4. Free energy density

We assume that W admits the additive decomposition

$$W(\mathbf{F}, C, C_\mathrm{s}, \mathbf{D}) = W_\mathrm{mec}(\mathbf{F}) + W_\mathrm{mix}(C, C_\mathrm{s}) + W_\mathrm{pol}(\mathbf{F}, \mathbf{D})\,, \tag{17}$$

in which W_mec, W_mix, and W_pol are the contributions due to the membrane stretching, the mixing of counterions and solvent molecules, and the membrane polarization, respectively.

To describe the mechanics of the membrane, we select the isotropic compressible Neo-Hookean material model proposed by Simo and Pister (1984):

$$W_{\text{mec}}(\mathbf{F}) = \frac{G}{2}(\text{tr}\,\mathbf{C} - 3) - G\ln J + \frac{1}{2}\lambda \ln^2 J\,, \tag{18}$$

in which $\lambda = E\nu/[(1+\nu)(1-2\nu)]$ and $G = E/[2(1+\nu)]$ are the Lamé parameters, with E and ν denoting the Young modulus and the Poisson ratio, and $\mathbf{C} = \mathbf{F}^{\text{T}}\mathbf{F}$ is the right Cauchy–Green deformation tensor. Eq. (18) describes a *coupled* hyperelastic material, that is, W_{mec} cannot be decomposed into the sum of isochoric and volumetric contributions (Holzapfel, 2000). This is known to be a desirable feature if one aims at capturing the large deformation behavior of elastomers (Boyce and Arruda, 2000). With respect to the material models usually employed in electrochemo-poromechanics, such that of Hong et al. (2010) for polyelectrolyte gels, the constitutive prescription in Eq. (18) involves an additional volumetric term modulated by λ. The use of both Lamé parameters allows a better tuning of the overall volumetric response, which is important for it influences the solvent flux, as demonstrated in Section 3 with particular reference to the counter-diffusion phenomena occurring in actuation and sensing. Cha and Porfiri (2014) also adopt a mechanical constitutive law involving both Lamé parameters, although they simply assume a Saint-Venant–Kirchhoff model for they are mainly interested in obtaining analytical solutions through asymptotic expansions, requiring appropriate linearizations. The importance of employing both Lamé parameters for the IPMC membrane has been unveiled by the study of Boldini and Porfiri (2020) on the multiaxial deformations experienced by IPMCs.

For the metal electrodes, we simply adopt the Saint-Venant–Kirchhoff isotropic material model:

$$W^{\text{e}}_{\text{mec}}(\mathbf{F}) = \frac{\lambda_{\text{e}}}{2}(\text{tr}\,\boldsymbol{\mathcal{E}})^2 + G_{\text{e}}\,\text{tr}\left(\boldsymbol{\mathcal{E}}^2\right),$$

in which λ_{e} and G_{e} are the Lamé parameters of the electrodes, whose Young modulus and Poisson ratio are E_{e} and ν_{e}, and $\boldsymbol{\mathcal{E}} = (\mathbf{C} - \mathbf{I})/2$ is the Green–Lagrange strain tensor.

We assume that the fluid phase behaves as an *ideal* solution of solvent and counterions, such that the free energy of mixing is purely entropic and reads (Ateshian, 2007)

$$W_{\text{mix}}(C, C_{\text{s}}) = RT\left(C\ln\frac{C}{C + C_{\text{s}}} + C_{\text{s}}\ln\frac{C_{\text{s}}}{C + C_{\text{s}}}\right), \tag{19}$$

in which R is the gas constant and T is the absolute temperature. We remark that Eq. (19) describes the mixing of solvent and counterions only, and this turns out to be consistent with an ideal mixture theory in which the solution of solvent and counterions identifies with the fluid phase (Ateshian, 2007), whereby we expect that the solid phase, consisting of the polymer chains, is much less relevant for mixing in IPMCs.[3] Under the assumption (2) of dilute fluid phase, Eq. (19) is substituted by the approximation

$$W_{\text{mix}}(C, C_{\text{s}}) = RTC\left(\ln\frac{C}{C_{\text{s}}} - 1\right). \tag{20}$$

We remark that our addition of the solvent mass balance (6) allows us to avoid the sophisticated modification of the Borukhov et al. (2000) mixing free energy proposed by Cha and Porfiri (2014), whose purpose is the inclusion in the theory of an osmotic stress related to the counterion electrodiffusion in the absence of the primal variable C_{s}. To this aim, the mixing free energy of Cha and Porfiri (2014) describes the interaction between the counterions and the polymer chains, resulting in an energy contribution dependent also on the deformation gradient $\mathbf{F}$. Then, Cha and Porfiri (2014) define the osmotic stress as the partial derivative of the mixing free energy density with respect to $\mathbf{F}$. Instead, in our framework, as specified in Eq. (13), we have a solvent pressure p_{s} entering both the stress and the solvent chemical potential μ_{s}, in addition to an osmotic contribution to μ_{s} deriving from the dependence of the mixing free energy (20) on C_{s}.

Finally, by following Hong et al. (2010), Cha and Porfiri (2014), and Zhang et al. (2020), we treat the membrane as an ideal dielectric, such that the polarization contribution reads

$$W_{\text{pol}}(\mathbf{F}, \mathbf{D}) = \frac{|\mathbf{FD}|^2}{2\varepsilon J}\,, \tag{21}$$

where ε is the absolute permittivity of the membrane.

2.5. Resulting conservative constitutive laws

2.5.1. Total stress tensor

By combining Eqs. (13)(a), (18), and (21), we obtain the *total* nominal stress

$$\mathbf{P} = \underbrace{G(\mathbf{F} - \mathbf{F}^{-\text{T}}) + \lambda \ln J\mathbf{F}^{-\text{T}}}_{\mathbf{P}_{\text{mec}}} \underbrace{-p_{\text{s}}J\mathbf{F}^{-\text{T}}}_{\mathbf{P}_{\text{s}}} + \underbrace{\frac{1}{2\varepsilon J}\left[2\mathbf{F}(\mathbf{D}\otimes\mathbf{D}) - \mathbf{C}\cdot(\mathbf{D}\otimes\mathbf{D})\mathbf{F}^{-\text{T}}\right]}_{\mathbf{P}_{\text{pol}}},$$

[3] For perspective, we briefly recall the mixing free energies proposed in the literature on the swelling of polymeric gels. Hong et al. (2008) and Chester and Anand (2010) account for the mixing of solvent with polymer macromolecules on the basis of the Flory–Huggins solution theory (Flory, 1942; Huggins, 1941). All the coupled interactions in the mixing of mobile ions, solvent, and polymer macromolecules are instead needed to accurately describe the swelling of polyelectrolyte gels (Hong et al., 2010; Zhang et al., 2020).

with $\otimes$ denoting the tensor product, such that $(\mathbf{D}\otimes\mathbf{D})_{IJ} = D_I D_J$. The corresponding total Cauchy stress is

$$\boldsymbol{\sigma} = \frac{1}{J}\mathbf{P}\mathbf{F}^{\mathrm{T}} = \underbrace{\frac{1}{J}[G(\mathbf{b}-\mathbf{I})+\lambda \ln J\mathbf{I}]}_{\boldsymbol{\sigma}_{\mathrm{mec}}} \underbrace{-p_{\mathrm{s}}\mathbf{I}}_{\boldsymbol{\sigma}_{\mathrm{s}}} + \underbrace{\frac{1}{2\epsilon}[2\mathbf{d}\otimes\mathbf{d}-(\mathbf{d}\cdot\mathbf{d})\mathbf{I}]}_{\boldsymbol{\sigma}_{\mathrm{pol}}}, \tag{22}$$

where $\mathbf{b} = \mathbf{F}\mathbf{F}^{\mathrm{T}}$ is the left Cauchy–Green deformation tensor and $\mathbf{d} = J^{-1}\mathbf{F}\mathbf{D}$ is the *current* electric displacement, that is, the electric displacement in the current configuration (Dorfmann and Ogden, 2005). The total pressure reads

$$p \equiv -\frac{1}{3}\mathrm{tr}\,\boldsymbol{\sigma} = \underbrace{-\frac{1}{J}\left[G\left(\frac{1}{3}\mathrm{tr}\,\mathbf{b}-1\right)+\lambda\ln J\right]}_{p_{\mathrm{mec}}} + p_{\mathrm{s}} + \underbrace{\frac{1}{6\epsilon}|\mathbf{d}|^2}_{p_{\mathrm{pol}}},$$

adopting the convention that each contribution to the pressure is positive if compressive.

In the jargon of poromechanics, $\boldsymbol{\sigma}_{\mathrm{mec}}$ and p_{s} are, respectively, the *effective* stress and the pore water pressure (Coussy, 2004; MacMinn et al., 2016). They should not be interpreted as the *partial* stresses of mixture theory associated with the solid and fluid phases (Bowen, 1980; Huyghe and Janssen, 1997; Ateshian, 2007). In electromechanics, $\boldsymbol{\sigma}_{\mathrm{pol}}$ is usually denoted as the Maxwell stress (Dorfmann and Ogden, 2005).

2.5.2. Electric displacement

By using Eqs. (10), (13)(b), and (21), we obtain the constitutive law for the nominal electric field, whose inversion provides the nominal electric displacement

$$\mathbf{D} = -\epsilon J\mathbf{C}^{-1}\nabla\psi\,.$$

As is well-known, in the current configuration, this relation reads $\mathbf{d} = -\epsilon\,\mathrm{grad}\,\psi$.[4]

2.5.3. Solvent and counterion (electro)chemical potentials

We obtain the solvent chemical potential by combining Eqs. (13)(c) and (20):

$$\mu_{\mathrm{s}} = -RT\frac{C}{C_{\mathrm{s}}} + v_{\mathrm{s}}p_{\mathrm{s}}\,. \tag{23}$$

Here, RTC should be interpreted as an osmotic contribution. In the Cha and Porfiri (2014) theory without steric effects (see, e.g., Boldini et al., 2020), this term is referred to as the osmotic pressure, contributing to the total stress.

Analogously, we obtain the counterion chemical potential μ by combining Eqs. (13)(d) and (20), thus leading to the counterion electrochemical potential of Eq. (11):

$$\tilde{\mu} = \underbrace{RT\ln\frac{C}{C_{\mathrm{s}}}}_{\mu} + F\psi\,. \tag{24}$$

We note that μ is unaffected by p_{s} because of the assumed negligibility of the volume occupied by counterions with respect to that of the solvent in the constraint (3).

2.6. Constitutive laws for the solvent and counterion fluxes

In order to obtain the expressions for $\mathbf{J}_{\mathrm{s}}$ and $\mathbf{J}$, we need to specify the mobility matrix $\boldsymbol{\mathcal{M}}$ introduced with Eq. (16). We adopt the form

$$\boldsymbol{\mathcal{M}} = \frac{1}{RT}\mathbf{C}^{-1}\begin{bmatrix} D_{\mathrm{s}}C_{\mathrm{s}} & D_{\mathrm{s}}C \\ D_{\mathrm{s}}C & \left(D_{\mathrm{s}}\dfrac{C}{C_{\mathrm{s}}}+D\right)C \end{bmatrix}, \tag{25}$$

in which D_{s} is the solvent diffusivity in the polymer network and D is the counterion diffusivity in the solvent. The matrix $\boldsymbol{\mathcal{M}}$ is positive definite for non-vanishing diffusivities and concentrations, thus fulfilling the dissipation inequality (14). Notably, our formulation of cross-diffusion is free from additional parameters with respect to the two diffusivities required for the self-diffusion. This differs from the cross-diffusion model proposed by Zhu et al. (2013), which requires a further drag coefficient.

In light of Eq. (25), Eqs. (15) become

$$\mathbf{J}_{\mathrm{s}} = -\frac{D_{\mathrm{s}}}{RT}\mathbf{C}^{-1}\left(C_{\mathrm{s}}\nabla\mu_{\mathrm{s}} + C\nabla\tilde{\mu}\right), \tag{26a}$$

$$\mathbf{J} = \frac{C}{C_{\mathrm{s}}}\mathbf{J}_{\mathrm{s}} - \frac{D}{RT}\mathbf{C}^{-1}C\nabla\tilde{\mu}\,. \tag{26b}$$

[4] The symbol grad denotes the spatial gradient, such that $(\mathrm{grad}\,\psi)_i = \partial\psi/\partial x_i$, where $\mathbf{x}$ indicates the current position vector.

We observe that Ateshian (2007) obtains flux equations analogous to Eqs. (26) within the mixture theory. Indeed, equations (128) and (129) of Ateshian (2007) are the counterpart in the current configuration of Eqs. (26a) and (26b), respectively, if one both assumes absence of friction between polymer chains and dilute species, as for instance in Huyghe and Janssen (1997), and considers that external body forces acting on solvent and dilute species vanish. We further note that, in order to describe the kinetics of polyelectrolyte gels, Zhang et al. (2020) follow the Maxwell–Stefan approach to mass transport in multicomponent systems (Krishna and Wesselingh, 1997), thus obtaining transport equations again corresponding to Eqs. (26).

Finally, combining Eqs. (23), (24), and (26) results in

$$\mathbf{J}_{\mathrm{s}} = -\frac{D_{\mathrm{s}}}{RT}\mathbf{C}^{-1}\left(v_{\mathrm{s}}C_{\mathrm{s}}\nabla p_{\mathrm{s}} + FC\nabla\psi\right), \tag{27a}$$

$$\mathbf{J} = \frac{C}{C_{\mathrm{s}}}\mathbf{J}_{\mathrm{s}} - D\mathbf{C}^{-1}\left(\nabla C - \frac{C}{C_{\mathrm{s}}}\nabla C_{\mathrm{s}} + \frac{FC}{RT}\nabla\psi\right). \tag{27b}$$

2.6.1. Discussion

Let us first focus on the solvent flux given by Eq. (27a). About the resolution strategy, we note that the use of constraints (3) and (4) allows us to express the solvent mass balance (6) in terms of the solvent pressure p_{s}. About the physics, we remark that, although the solvent is assumed to be electrically neutral, its flux depends on the electric potential gradient. In particular, the last term in Eq. (27a) represents the solvent *electro-osmotic* flux, which is recognized by many investigators as a fundamental mechanism of solvent transport in IPMC actuation (Asaka and Oguro, 2000; Shahinpoor and Kim, 2004; Zhu et al., 2013). Indeed, as a voltage drop is applied across the electrodes, counterions migrate in the direction of the electric field, carrying along solvent molecules proportionally to the counterion concentration.

In the limit case of absence of counterions, the volumetric nominal flux of solvent $\mathbf{J}_{\mathrm{s}}^{\mathrm{v}}$, through Eq. (27a), reads

$$\mathbf{J}_{\mathrm{s}}^{\mathrm{v}} = v_{\mathrm{s}}\mathbf{J}_{\mathrm{s}} = -J\mathbf{C}^{-1}\frac{D_{\mathrm{s}}\varphi_{\mathrm{s}}^2}{RTc_{\mathrm{s}}}\nabla p_{\mathrm{s}},$$

where we have introduced the current solvent concentration $c_{\mathrm{s}} = C_{\mathrm{s}}/J$ and the current porosity $\varphi_{\mathrm{s}} = v_{\mathrm{s}}c_{\mathrm{s}}$. Then, by defining the permeability of the polymer network to the solvent in terms of the solvent diffusivity as $k_{\mathrm{s}} = D_{\mathrm{s}}\varphi_{\mathrm{s}}^2/(RTc_{\mathrm{s}})$, one obtains the nominal version of Darcy law (MacMinn et al., 2016):

$$\mathbf{J}_{\mathrm{s}}^{\mathrm{v}} = -J\mathbf{C}^{-1}k_{\mathrm{s}}\nabla p_{\mathrm{s}},$$

whose more common counterpart in the current configuration reads $\mathbf{j}_{\mathrm{s}}^{\mathrm{v}} = -k_{\mathrm{s}}\,\mathrm{grad}\,p_{\mathrm{s}}$.

By focusing now on the counterion flux in Eq. (27b), we note that, in our framework, $\mathbf{J}_{\mathrm{s}}/C_{\mathrm{s}}$ is related to the velocity of solvent molecules with respect to the polymer network (see also Ateshian, 2007, equation (129)). Therefore, the first addend represents the *convective* flux of counterions with the solvent (see, e.g., equation (1.4.2) of Bard and Faulkner, 2001). Within our theory, it constitutes an important contribution of counterion flux in sensing, as also in Zhu et al. (2016). Indeed, upon application of a mechanical stimulus, the solvent moves down its pressure gradient, carrying along some counterions. Moreover, within this motion, the solvent establishes a volumetric deformation gradient (see Eq. (3)), which triggers counterion diffusion; this is considered through the third term in Eq. (27b), proportional to $\nabla C_{\mathrm{s}} = \nabla J/v_{\mathrm{s}}$. Counterion convection along $\mathbf{J}_{\mathrm{s}}$ and diffusion along ∇C_{s} originate an ion imbalance and, consequently, an electric signal. Our theory explains the weak response characterizing IPMC sensors (Shahinpoor and Kim, 2004) with the smallness of the two foregoing contributions to the counterion flux, both proportional to $C \ll C_{\mathrm{s}}$.

Finally, in the limit case of immobile solvent (that is, $D_{\mathrm{s}} = 0$, also implying $\mathbf{J}_{\mathrm{s}} = \mathbf{0}$ through Eq. (27a)), we have $C_{\mathrm{s}} = C_{\mathrm{s}}^0$ (Eq. (6)), $J = 1$ (Eq. (3)), $c = C$, and $c_{\mathrm{s}} = C_{\mathrm{s}}$, such that Eq. (27b) reduces to

$$\mathbf{J} = -D\mathbf{C}^{-1}\left(\nabla C + \frac{FC}{RT}\nabla\psi\right),$$

whose counterpart in the current configuration reads $\mathbf{j} = -D\left[\mathrm{grad}\,c + Fc/(RT)\,\mathrm{grad}\,\psi\right]$, which is the classical Nernst–Planck law (Porfiri, 2008), stating that both the gradient of the counterion concentration (Fick effect) and the electric field (electrophoretic effect) concur to the counterion transport.

3. Analysis of actuation and sensing

Here, we investigate the mechanisms underlying actuation and sensing on the basis of finite element solutions of the proposed model applied to the benchmarks depicted in Fig. 1.

3.1. Model parameters

We consider a typical IPMC of length $L = 20\,\mathrm{mm}$, membrane thickness $2H = 200\,\mu\mathrm{m}$, and electrode thickness $h = 1\,\mu\mathrm{m}$. With reference to a saturated Nafion membrane, we adopt $G = 50\,\mathrm{MPa}$ and, unless otherwise specified, $\lambda = 300\,\mathrm{MPa}$ for the Lamé parameters (Silberstein and Boyce, 2010), such that $K \approx 333\,\mathrm{MPa}$, $\nu \approx 0.4286$, and $E \approx 143\,\mathrm{MPa}$. The Lamé parameters of the electrodes are two orders of magnitude larger, that is, $G_{\mathrm{e}} = 5\,\mathrm{GPa}$ and $\lambda_{\mathrm{e}} = 30\,\mathrm{GPa}$. With respect to the usual moduli for metals,

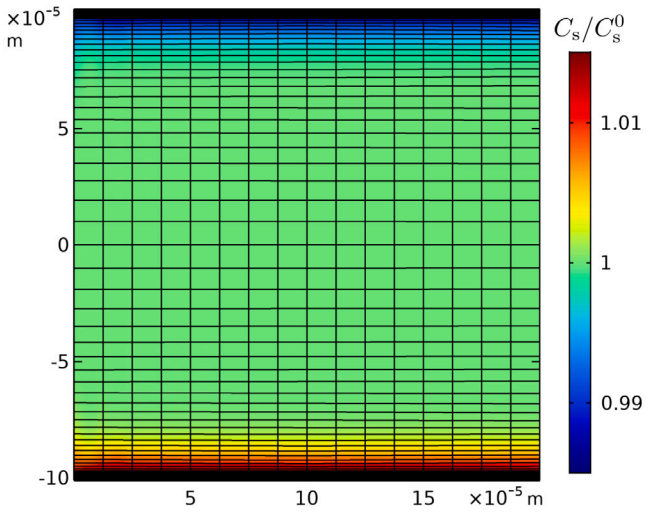

Fig. 2. Finite element mesh at the clamped end region of the membrane, with the non-dimensional solvent concentration $C_s(X,Y)/C_s^0$ for the actuation problem (Section 3.3) at the analysis instant $t = 0.1$ s. (For interpretation of the references to color in this figure legend, the reader is referred to the web version of this article.)

these are about one order of magnitude lower (Liu et al., 2019), as justified by their significantly larger defectiveness, due to the plating processes adopted in IPMC fabrication (Kim and Shahinpoor, 2003).

We adopt room temperature $T = 300\,\mathrm{K}$ and water as solvent, such that $v_s = 18\,\mathrm{cm}^3/\mathrm{mol}$. We select $C_s^0 = 20\,000\,\mathrm{mol/m}^3$ (corresponding to initial volume fraction of water $v_s C_s^0 = 0.36$), $D_s = 10^{-9}\,\mathrm{m}^2/\mathrm{s}$, $D = 10^{-10}\,\mathrm{m}^2/\mathrm{s}$, $C^0 = 1200\,\mathrm{mol/m}^3$, and $\varepsilon = 10^{-4}\,\mathrm{F/m}$. These values are within the ranges proposed by Zhu et al. (2016).

3.2. Finite element model

The finite element solution is obtained with the commercial software *COMSOL Multiphysics*® under plane strain conditions. We adopt the `General Form PDE` interface to solve the governing equations ensuing from the mass balances and the Gauss law, by employing quadratic Lagrangian shape functions to approximate the fields p_s, C, and ψ. We use the `Solid Mechanics` interface to solve the equilibrium equations, by choosing quadratic serendipity shape functions to approximate the field $\mathbf{u}$.

The mesh consists of 19 565 quadrilateral elements, whose geometry is described by quadratic serendipity shape functions. We discretize the IPMC length (X direction) with 200 uniform elements of size 0.1 mm each, except for a region of width $2H = 0.2$ mm at the clamped end, where we employ a finer mesh featuring 16 columns of elements instead of 2; this mesh region, required to obtain a sufficiently accurate deformation field therein, is displayed in Fig. 2. We discretize the membrane thickness (Y direction) with 50 elements, whose size decreases from the center to the electrodes in geometric sequence with the ratio between the largest and the smallest elements equal to 10; in the electrodes the mesh is uniform, featuring 4 elements along the thickness. We additionally introduce 16 `boundary layer` elements in each of the membrane regions next to the electrodes. These elements also have variable size along the Y direction, with the smallest ones, adjacent to the electrodes, of size 10 nm, and the stretching factor between two consecutive elements equal to 1.2. These very fine mesh regions are motivated by the large gradients of C and ψ therein, which constitute the well-established essential feature of IPMC electrochemistry (Porfiri, 2008), in our poromechanical model accompanied by the gradient of C_s. The overall number of degrees of freedom is 329 133.

We employ Backward Differentiation Formula for the time integration. At each time step, we use a `segregated` approach to solve the discretized equations. Specifically, in actuation we first solve the electrochemical problem, and then, in an iterative loop, use this solution to inform and solve the poromechanical problem. Dually, in sensing the algorithm first solves the poromechanical problem, and then uses the obtained solution as a guess for the electrochemical problem. These solution schemes are convenient as they are suggested by the underlying physics.

While the response is almost independent of X in actuation, the maximum electrochemical response in sensing is obtained in the cross-section where the bending moment attains its maximum value out of the region influenced by the fully clamped constraint, that is, at $X \simeq L/100$. Our finite element model allows us to obtain accurate results within this cross-section, where, in the following, we discuss the through-the-thickness variation of the relevant fields.[5]

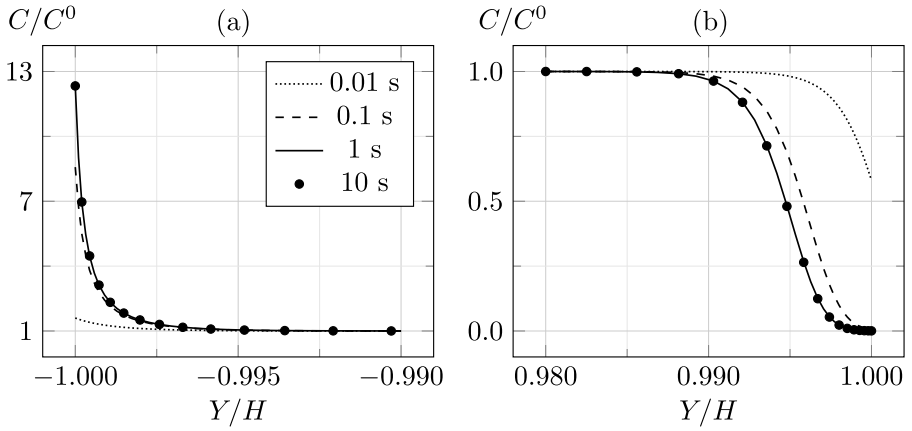

Fig. 3. Actuation: non-dimensional counterion concentration $C(Y)/C^0$ at $X = L/100$ in the cathode (a) and anode (b) boundary layers.

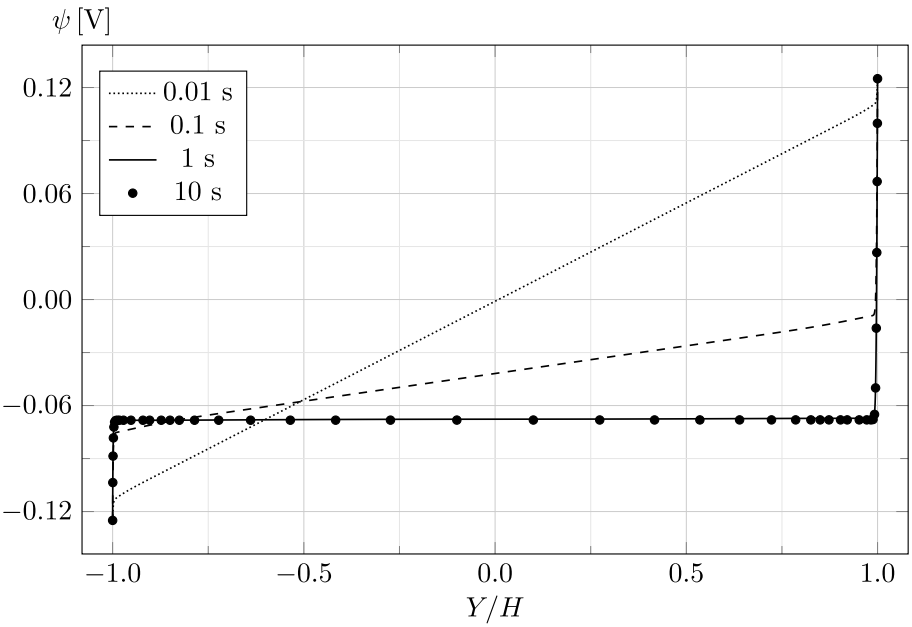

Fig. 4. Actuation: electric potential $\psi(Y)$ at $X = L/100$ in the membrane.

3.3. Actuation

In actuation, the numerical model allows us to instantaneously apply a voltage drop $\bar{\psi} = 0.25\,\mathrm{V}$ across the electrodes, which is then maintained until the steady state. This elicits the counterion migration from the anode to the cathode, resulting in counterion depletion and accumulation in the boundary layers, with the membrane bulk remaining electroneutral. In Fig. 3 we display the counterion concentration $C(Y)$ in the boundary layers, at different time instants. At the cathode, C increases up to about $12\,C^0$ at $t \approx 1$ s, and then remains constant. At the anode, C decreases to zero at $t \approx 0.1$ s, and then the thickness of the boundary layer increases until $C(Y)$ attains its steady state profile at $t \approx 1$ s. As displayed in Fig. 4, the asymmetry of the boundary layers reflects on the electric potential $\psi(Y)$, which, through the Maxwell stress, is relevant for the back-relaxation (Porfiri et al., 2017). Importantly, the reason for the highlighted asymmetry is inherently electrochemical, although it is strengthened by large deformations.

As counterions migrate toward the cathode, the solvent molecules follow by electro-osmosis. In Figs. 5 and 6 we represent $C_s(Y)$ in the boundary layers and in the membrane bulk, respectively. In the cathode boundary layer, the peak value of C_s increases up

[5] Analyzing the results so close to the fully clamped cross-section is convenient also because of its very small rotation, leading to negligible difference between its normal in the reference and current configurations.

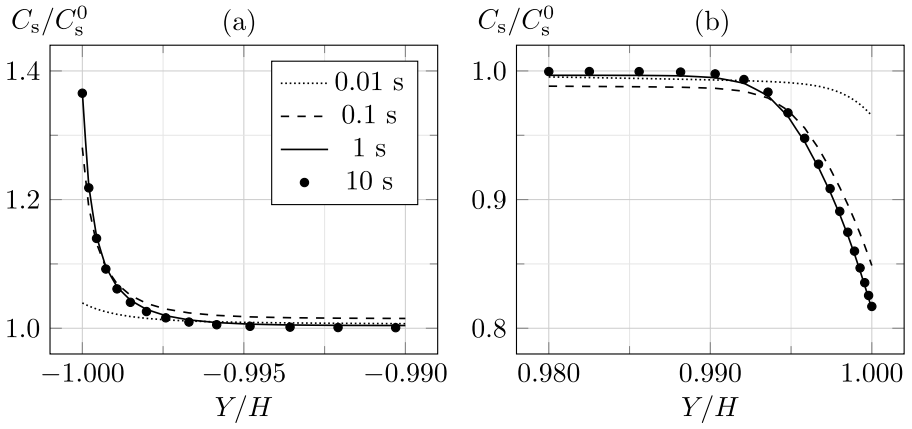

Fig. 5. Actuation: non-dimensional solvent concentration $C_s(Y)/C_s^0$ at $X = L/100$ in the cathode (a) and anode (b) boundary layers.

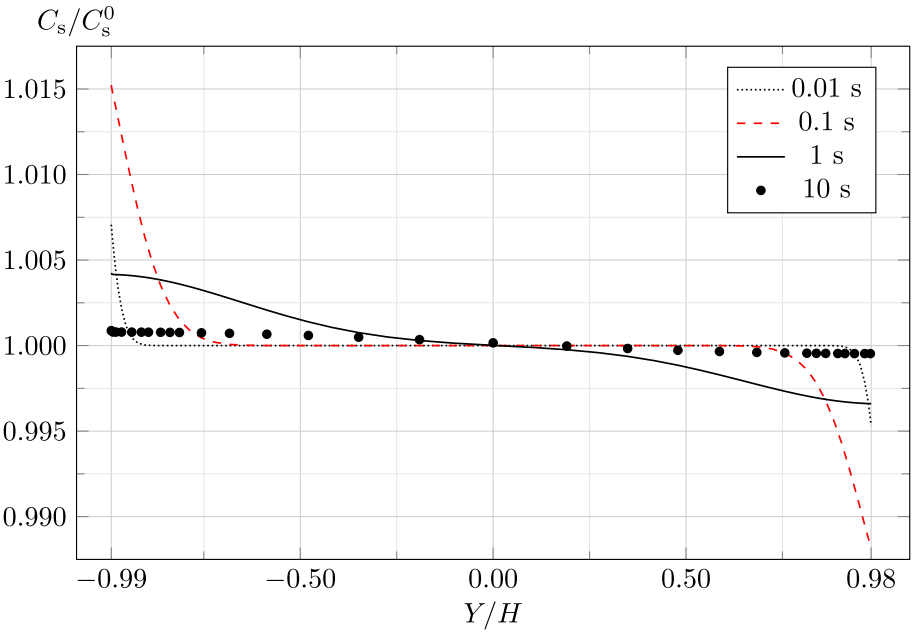

Fig. 6. Actuation: non-dimensional solvent concentration $C_s(Y)/C_s^0$ at $X = L/100$ in the membrane bulk (boundary layers excluded). The curve corresponding to the time instant $t \approx 0.1$ s at which the solvent begins counter-diffusing is highlighted in red. (For interpretation of the references to color in this figure legend, the reader is referred to the web version of this article.)

to about $1.36\,C_s^0$ at $t \approx 1$ s, and then remains constant. Outside the cathode boundary layer, C_s increases until $t \approx 0.1$ s, and then slowly decreases, by approaching its initial value at the steady state. The anode side behaves similarly, though experiencing solvent depletion. The contour of C_s in the clamped region of the membrane at $t = 0.1$ s is further reported in previous Fig. 2, where the color bar is set in such a way as to highlight the variation of C_s in the membrane bulk, thus obscuring its variation in the boundary layers, as in Fig. 6. Analogously to C, we note that the maximum solvent accumulation at the cathode, characterized by a thinner boundary layer, is larger than the maximum depletion at the anode, indicating asymmetry in the solvent redistribution. Notably, the relative change of C_s along the membrane thickness is much lower than that of C (compare, e.g., the profiles at the cathode in Figs. 3(a) and 5(a)).

We draw the first conclusion that in the boundary layers (Fig. 5) the contribution of the solvent pressure gradient ∇p_s to the solvent flux never exceeds that of the electric field $\mathbf{E}$, such that C_s undergoes a monotonic variation in time until the steady state. In other words, in IPMC actuation, the electrochemistry also governs the boundary layer behavior of the solvent. Instead, in the membrane bulk (Fig. 6), the contribution of ∇p_s overcomes that of $\mathbf{E}$ at a certain instant, after which the solvent counter-diffuses and back-relaxation occurs.

For the flexure magnitude, in Fig. 7 we display the time evolution of the transverse displacement $u_Y(L, 0)$. It initially rapidly increases, reaching the peak value u_Y^{p} at t^{p}. Then back-relaxation occurs and u_Y slowly decreases until the steady state value u_Y^{ss} at

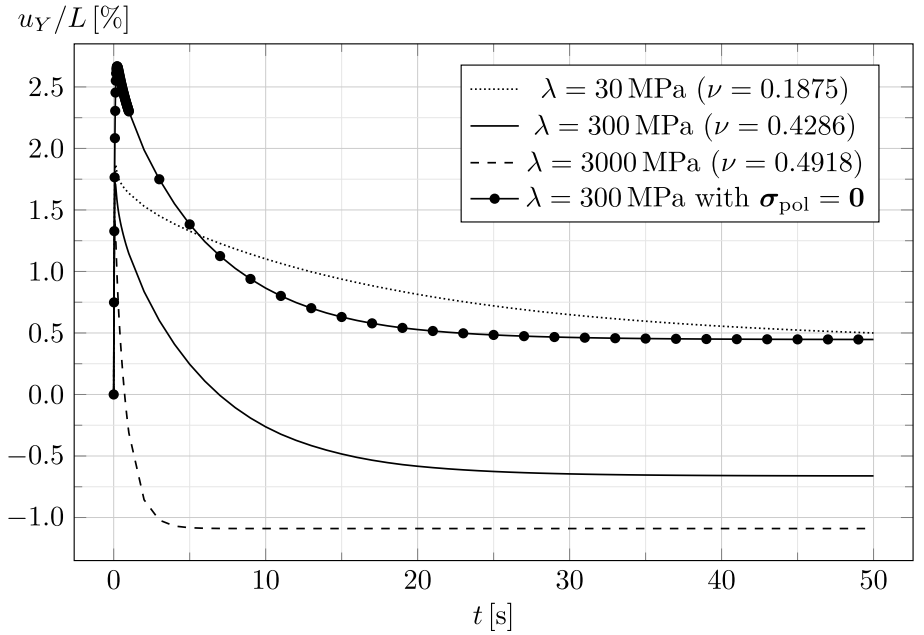

Fig. 7. Actuation: non-dimensional transverse displacement $u_Y(t)$ evaluated at the free end $(X, Y) = (L, 0)$.

t^{ss}. With reference to the case $\lambda = 300\,\mathrm{MPa}$: $u_Y^{\mathrm{p}} \approx 1.7\%\, L$, $t^{\mathrm{p}} \approx 0.1$ s and $u_Y^{\mathrm{ss}} \approx -0.7\%\, L$, $t^{\mathrm{ss}} \approx 50$ s. Therefore, while initially the IPMC bends toward the anode, it finally undergoes opposite curvature, bending toward the cathode. This behavior and the associated timescales were first documented in Asaka et al. (1995).

Remarkably, as shown in Fig. 7 and demonstrated in the following, disregarding the Maxwell stress both leads to a significant overestimation of u_Y^{p} ($u_Y^{\mathrm{p}} \approx 2.7\%\, L$, now reached at $t^{\mathrm{p}} \approx 0.25$ s) and excludes the possibility of predicting the change in sign of the curvature, although back-relaxation still takes place.

Fig. 7 also displays the dependence of the back-relaxation on the first Lamé parameter λ, whereby increasing λ anticipates the steady state and amplifies the magnitude of the back-relaxation. Moreover, it exists a sufficiently small λ such that the curvature does not change sign, although back-relaxation still occurs. We can explain this dependence of the flexure on λ by leveraging on the two fundamental results illustrated below.

First, as illustrated in Fig. 8, the longitudinal (Green–Lagrange) strain $\mathcal{E}_{XX}(Y)$ remains nearly linear all along the IPMC cross-section. On this basis, let us note that Fig. 8 clearly reports the change of curvature sign at the steady state with respect to that at the initial peak. In more detail, at t^{p} the IPMC bends toward the anode and the neutral axis is shifted, with respect to the mid-axis, toward the anode. At t^{ss} the curvature has opposite sign, with the IPMC bending now toward the cathode; notably, the whole cross-section presents positive $\mathcal{E}_{XX}$, denoting a longitudinal elongation of the strip. The IPMC extension under actuation has also been reported in Boldini et al. (2020) on the basis of the Cha and Porfiri (2014) theory. Generally, $\mathcal{E}_{XX}$ is small, although the bending deformation is relevant, given the strip slenderness. In Fig. 9 we report the undeformed configuration and the deformed configurations at t^{p} and t^{ss}, with the associated contour plots of $\mathcal{E}_{XX}$.

Second, it is crucial to notice, as documented by Fig. 10, how the Maxwell stress $\sigma_{yy}^{\mathrm{pol}}(Y) \equiv -\sigma_{xx}^{\mathrm{pol}}(Y)$ grows asymmetrically in the boundary layers. Since $\partial\psi/\partial x$ is negligible, $\sigma_{yy}^{\mathrm{pol}} \approx (\varepsilon/2)(\partial\psi/\partial y)^2$ has the same sign on both sides of the membrane, where it increases in magnitude with time. Importantly, near the anode $\sigma_{yy}^{\mathrm{pol}}$ assumes slightly greater values and, most of all, it attains a relevant magnitude in a larger region, because of the thicker boundary layer therein. This asymmetry grows with time, and is expected to increase with the applied voltage (Porfiri et al., 2017).

Hence, we can explain the mechanics behind the back-relaxation documented in Fig. 7 by temporarily resorting to small strains and decoupling poromechanics and electrochemistry, solving the latter first. This provides, by suitably approximating the behavior observed in Fig. 8, a longitudinal strain $\varepsilon_{xx}(y) \approx \kappa y + \varepsilon_0$, with κ denoting the curvature and ε_0 the mid-axis strain, and a known Maxwell stress $\sigma_{yy}^{\mathrm{pol}}(y) \approx (\varepsilon/2)(\partial\psi/\partial y)^2$. Then, by resorting to the equilibrium along y, we can estimate the transverse mechanical stress $\sigma_{yy}^{\mathrm{mec}}(y) \approx -\sigma_{yy}^{\mathrm{pol}}(y) + p_{\mathrm{s}}(y)$, as confirmed by the finite element analyses. Under plane strain, the longitudinal mechanical stress reads $\sigma_{xx}^{\mathrm{mec}}(y) = [E/(1-\nu^2)]\varepsilon_{xx}(y) + [\nu/(1-\nu)]\sigma_{yy}^{\mathrm{mec}}(y)$, such that the *total* longitudinal stress in the membrane turns out to be

$$\sigma_{xx}(y) \approx \frac{E}{1-\nu^2}(\kappa y + \varepsilon_0) + \frac{\nu}{1-\nu}\left[-\sigma_{yy}^{\mathrm{pol}}(y) + p_{\mathrm{s}}(y)\right] - \sigma_{yy}^{\mathrm{pol}}(y) - p_{\mathrm{s}}(y)\,. \tag{28}$$

In the electrodes, we simply have

$$\sigma_{xx}(y) \equiv \sigma_{xx}^{\mathrm{mec}}(y) \approx \frac{E_{\mathrm{e}}}{1-\nu_{\mathrm{e}}^2}(k y + \varepsilon_0)\,. \tag{29}$$

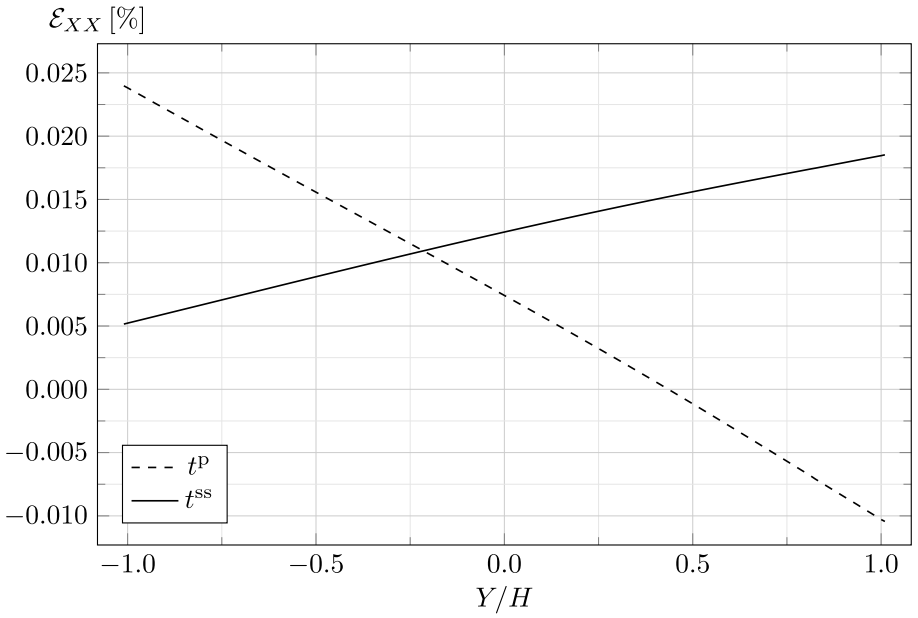

Fig. 8. Actuation: longitudinal strain $\mathcal{E}_{XX}(Y)$ at $X = L/100$ in the membrane and electrodes.

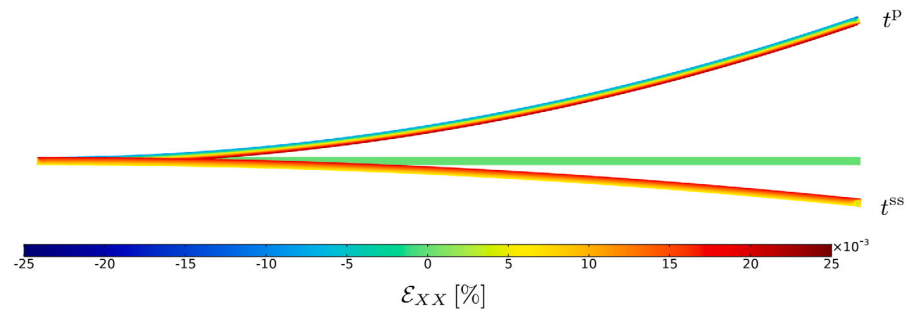

Fig. 9. Actuation: undeformed configuration and deformed configurations (10 times amplified) at t^{p} and t^{ss}, also displaying the longitudinal strain field $\mathcal{E}_{XX}$. (For interpretation of the references to color in this figure legend, the reader is referred to the web version of this article.)

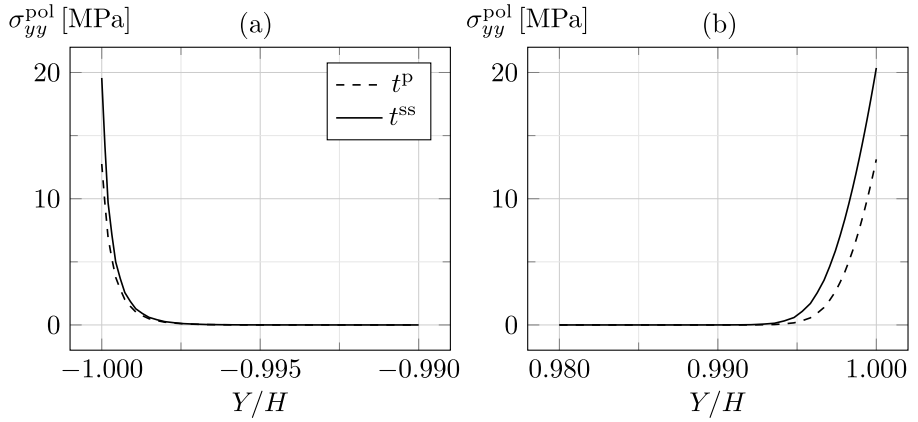

Fig. 10. Actuation: transverse Maxwell stress $\sigma_{yy}^{\mathrm{pol}}(Y)$ at $X = L/100$ in the cathode (a) and anode (b) boundary layers.

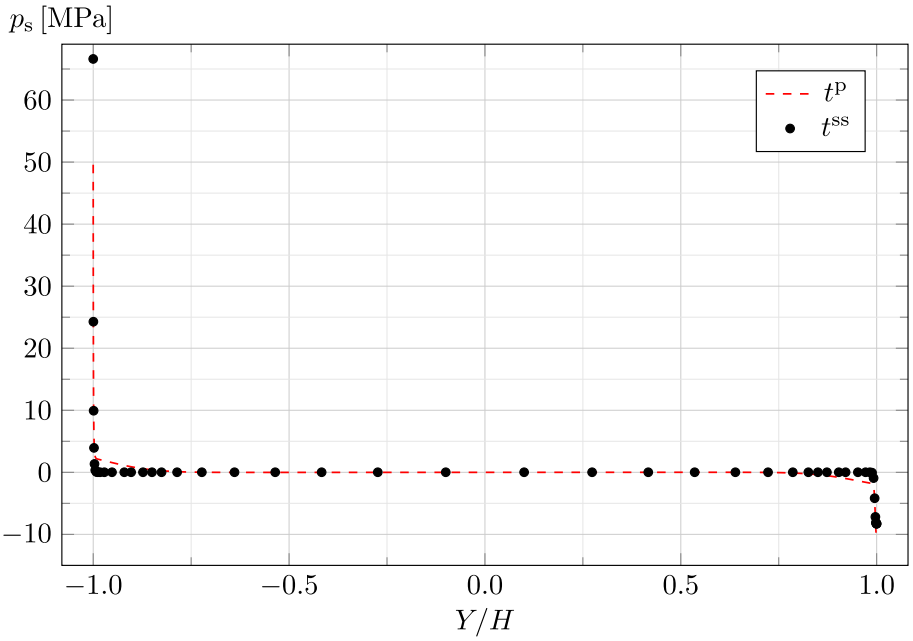

Fig. 11. Actuation: solvent pressure $p_s(Y)$ at $X = L/100$ in the membrane.

Since no mechanical loads are applied to the IPMC in actuation, we can estimate κ and ε_0 by imposing vanishing total bending moment and total axial force. In particular, by using Eqs. (28) and (29), the first condition provides

$$\kappa \approx \frac{1}{\beta(1-\nu)} \int_{-H}^{H} [\sigma_{yy}^{\mathrm{pol}}(y) + (1-2\nu)p_s(y)]y \,\mathrm{d}y = -\frac{1}{\beta(1-\nu)} \left[M_{\mathrm{pol}} + (1-2\nu)M_s\right] , \tag{30}$$

where

$$\beta = \frac{E}{1-\nu^2}\frac{2}{3}H^3 + \frac{E_e}{1-\nu_e^2}2H^2h \tag{31}$$

is the plane strain bending stiffness per unit depth relying on the Bernoulli–Navier kinematics and on the assumption of *thin skins*, and M_{pol} and M_s are the bending moments per unit depth due to the Maxwell stress and to the solvent pressure. It is important to notice that, in Eq. (30), the difference from unity of the coefficients $(1-\nu)$ and $(1-2\nu)$ ensues from the second contribution to the *mechanical* stress in Eq. (28), which has been overlooked so far in IPMC literature, to the best of our knowledge.

Given that the solvent moves from the anode to the cathode, Eq. (30) establishes that the solvent pressure always gives a negative contribution to κ, corresponding to bending toward the anode. In fact, as shown in Fig. 11, at the anode side (where $y > 0$) $p_s < 0$ and at the cathode side (where $y < 0$) $p_s > 0$.

Instead, the Maxwell stress $\sigma_{yy}^{\mathrm{pol}} > 0$ gives a positive contribution to κ at the anode side, while it provides a negative contribution to κ at the cathode side. Therefore, the back-relaxation may lead to bending toward the cathode ($\kappa > 0$) only due to the Maxwell stress, whereby this occurs when the contribution of the Maxwell stress at the anode overcomes those of the solvent pressure and of the Maxwell stress at the cathode. This turns out to be possible because of the boundary layers asymmetry described above (see, in particular, Fig. 10).

Moreover, Eq. (30) allows us to explain the back-relaxation dependence on λ, as illustrated in Fig. 7: increasing λ for a given G implies a larger ν, the latter approaching 0.5 as $\lambda \to \infty$; this diminishes the negative contribution to κ due to p_s, thus anticipating and emphasizing the back-relaxation.

Let us now delve into further details on the back-relaxation contribution due to the solvent counter-diffusion, on the basis of $p_s(Y)$ in Fig. 11. In passing from t^p to t^{ss}, p_s diminishes everywhere, except for the cathode boundary layer, resulting in a decrease of M_s with time, as confirmed by the case disregarding the Maxwell stress in Fig. 7. Notably, in this latter case, if $\lambda \to \infty$ at fixed G, then $\nu \to 0.5$ and the steady state curvature approaches zero, as revealed by Eq. (30).

As recently established by Boldini and Porfiri (2020) and Boldini et al. (2020), the IPMC actuation is characterized by large gradients of all the relevant stress and strain components in the boundary layers, except for the longitudinal strain (see Fig. 8). This is detailed in the following within the context of the present theory. Fig. 12 displays the transverse Green–Lagrange strain $\mathcal{E}_{YY}(Y)$ at the cathode and anode sides, respectively. The profile of $\mathcal{E}_{YY}$ is asymmetric, with the peak magnitude of $\mathcal{E}_{YY}$ at the cathode being nearly double than that at the anode. The poromechanical framework allows the model to further predict non-negligible $\mathcal{E}_{YY}$ outside the boundary layers, which vanishes at the steady state, according to the solvent redistribution (see Fig. 6).

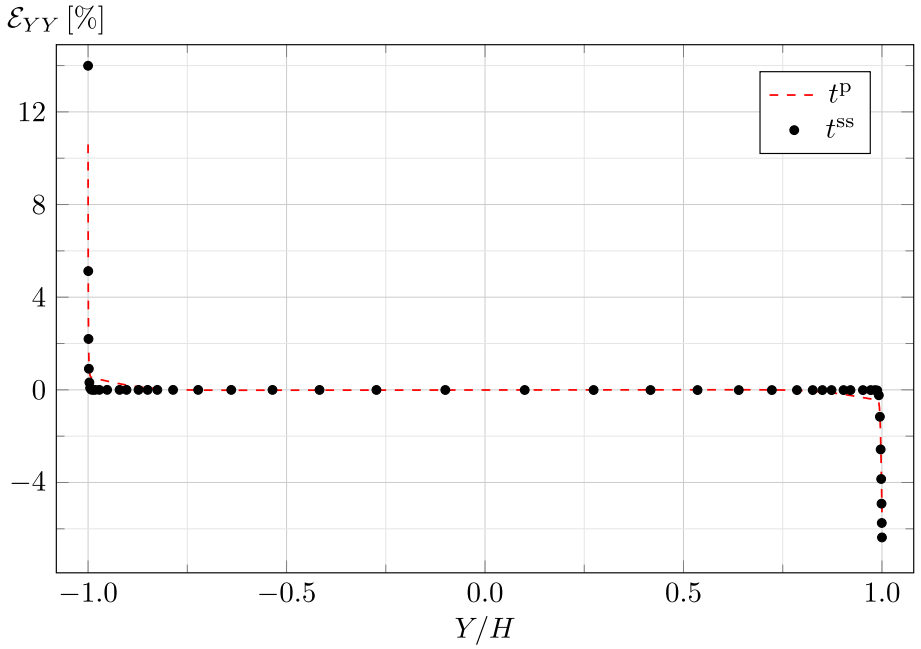

Fig. 12. Actuation: transverse strain $\mathcal{E}_{YY}(Y)$ at $X = L/100$ in the membrane.

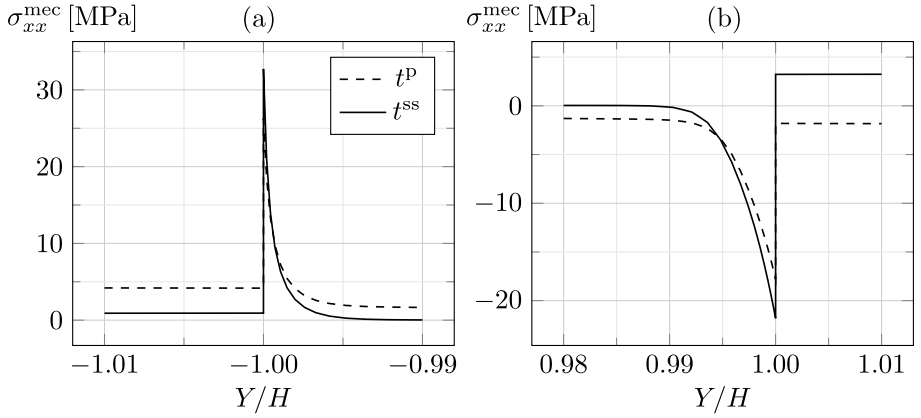

Fig. 13. Actuation: longitudinal mechanical stress $\sigma_{xx}^{\mathrm{mec}}(Y)$ at $X = L/100$ in the cathode (a) and in the anode (b), including the boundary layers in the membrane.

Finally, in Fig. 13 we represent the longitudinal mechanical stress $\sigma_{xx}^{\mathrm{mec}}(Y)$ at the cathode and anode sides. It is worth noting that the steady state bending toward the cathode, due to back-relaxation, is accompanied with a change in sign of the axial stress in the anode, which becomes larger than that at the cathode. Remarkably, $\sigma_{xx}^{\mathrm{mec}}$ and $\sigma_{yy}^{\mathrm{mec}}$ combine as to provide a longitudinal strain that is well approximated by an affine function of Y.

In Porfiri et al. (2017) the importance of the Maxwell stress in IPMC back-relaxation was first advanced, on the basis of the Cha and Porfiri (2014) theory, which neglects the solvent flow, and assumes that actuation is triggered by an osmotic pressure term proportional to the counterion concentration. Given that counterions are unlikely to counter-diffuse in actuation, in the Cha and Porfiri (2014) framework the back-relaxation can be explained exclusively through electrostatic arguments. Conversely, Zhu et al. (2013) account for the cross-diffusion of solvent and counterions, but neglect the Maxwell stress; indeed, Zhu et al. (2013) predict back-relaxation without reversal of the curvature.

The present theory is, to the best of our knowledge, the first one to effectively combine the classical model of the back-relaxation, based on the solvent counter-diffusion, with the more recent (so far, alternative) description relying on the relevance of the Maxwell stress. Furthermore, our theory allows one to establish a precise link between the steady state bending response and the Lamé constants, thus suggesting a possible strategy for the identification of the model parameters.

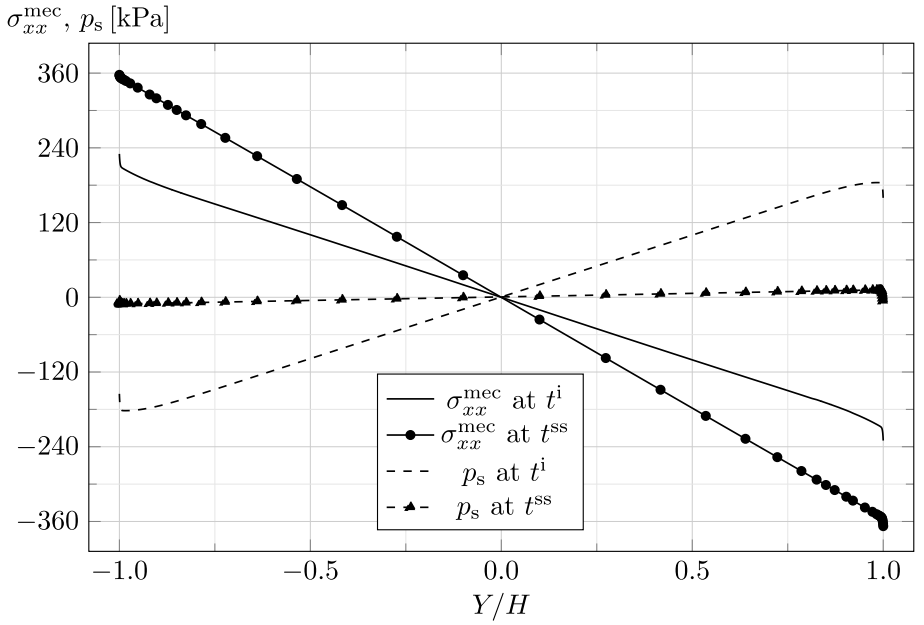

Fig. 14. Sensing: longitudinal mechanical stress $\sigma_{xx}^{\mathrm{mec}}(Y)$ and solvent pressure $p_{\mathrm{s}}(Y)$ at $X = L/100$ in the membrane.

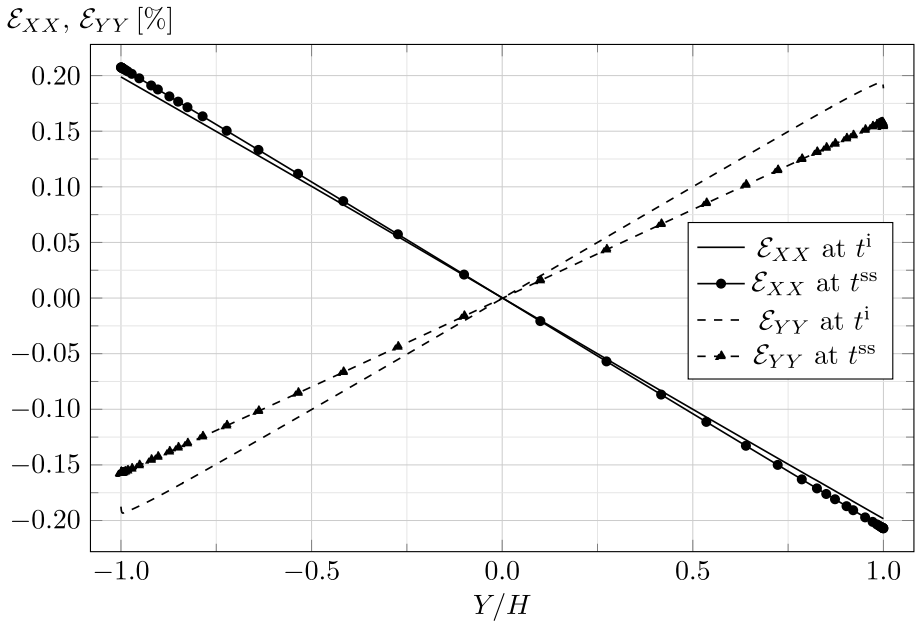

Fig. 15. Sensing: longitudinal, $\mathcal{E}_{XX}(Y)$, and transverse, $\mathcal{E}_{YY}(Y)$, strains at $X = L/100$ in the membrane.

3.4. Sensing

In short-circuit sensing, we impose a uniformly distributed nominal load of magnitude $\overline{T} = 50\,\mathrm{N/m^2}$. The numerical model does not allow us to instantaneously apply this load; hence, we linearly enforce it in a suitably short time interval $t^{\mathrm{i}} = 0.1$ s, and then maintain it until the steady state. This leads to a sensing response triggered by poromechanics, as described in the following.

In Fig. 14 we represent the longitudinal mechanical stress $\sigma_{xx}^{\mathrm{mec}}$ and the solvent pressure p_{s} along the membrane thickness, at $t^{\mathrm{i}} = 0.1$ s and $t^{\mathrm{ss}} \approx 50$ s. While $|\sigma_{xx}^{\mathrm{mec}}|$ increases in time, $|p_{\mathrm{s}}|$ decreases and nearly vanishes everywhere at the steady state. At each time

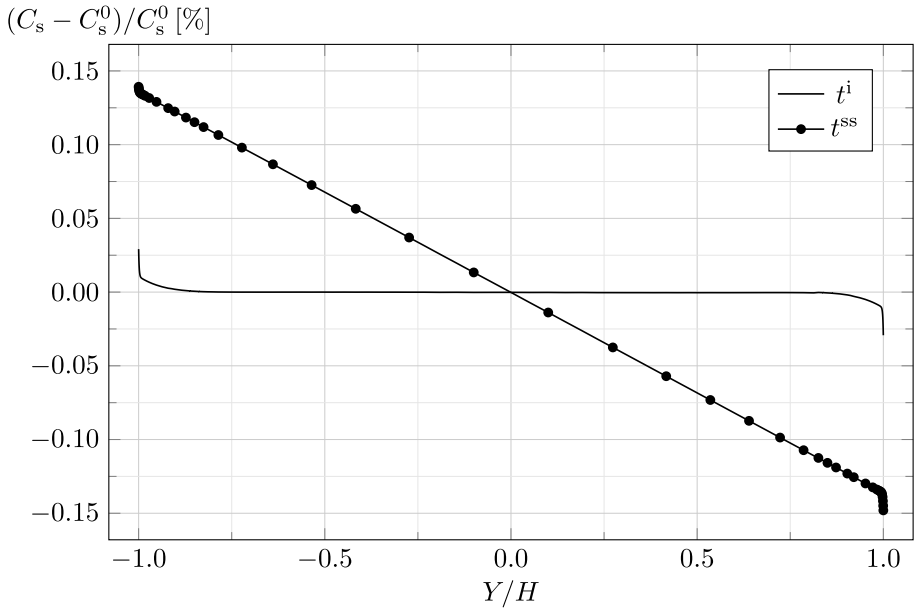

Fig. 16. Sensing: relative solvent concentration $\left[C_s(Y) - C_s^0\right]/C_s^0$ at $X = L/100$ in the membrane.

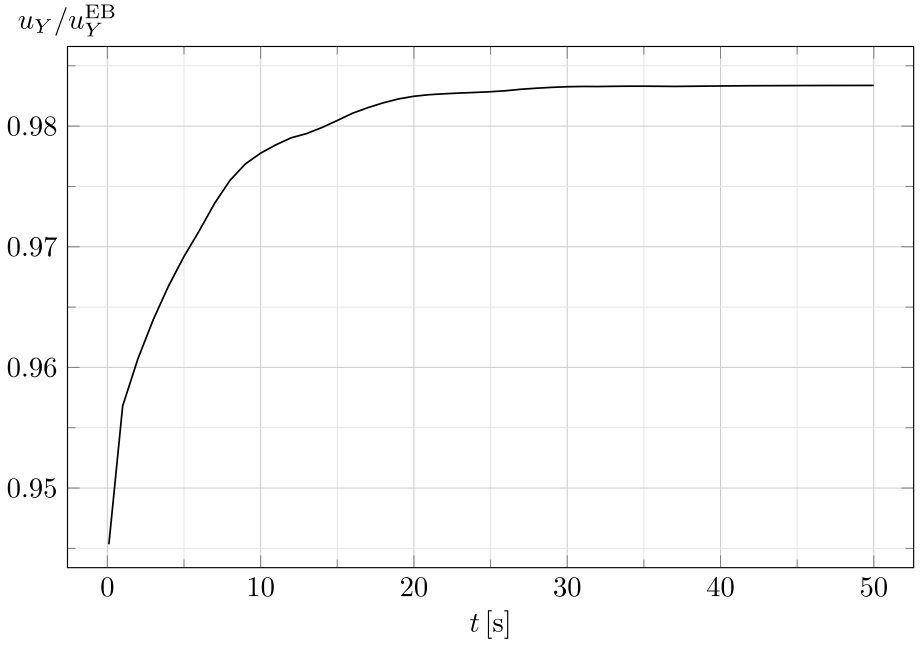

Fig. 17. Sensing: non-dimensional transverse displacement $u_Y(t)$ at $(X, Y) = (L, 0)$ relative to the value u_Y^{EB} predicted by the linear elastic Euler–Bernoulli beam model.

instant, we observe that $\sigma_{xx}^{mec}(t) - p_s(t) \approx \sigma_{xx}^{mec}(t^{ss})$, showing, incidentally, that the time evolution of the Maxwell stress is irrelevant. In Fig. 15 we display the longitudinal, $\mathcal{E}_{XX}$, and transverse, $\mathcal{E}_{YY}$, Green–Lagrange strains. The cathode side extends longitudinally and shortens transversely, while the anode side exhibits opposite behavior. Progressively, $|\mathcal{E}_{XX}|$ slightly increases, while $|\mathcal{E}_{YY}|$ decreases. In Fig. 16 we represent the solvent concentration C_s, which is directly related to the volumetric deformation by Eq. (3). It increases with time at the cathode side while decreasing at the anode side. All the poromechanical fields are nearly symmetric with respect to the mid-axis, except for some asymmetry arising in the boundary layers as the steady state is approached.

In Fig. 17 we represent the time evolution of the transverse displacement at the free end, $u_Y(L, 0)$, which is non-dimensionalized through its value estimated with the linear elastic Euler–Bernoulli beam theory $u_Y^{EB} = \overline{T} L^4/(8\beta) \approx 2.14\,\text{mm}$, where β is given by

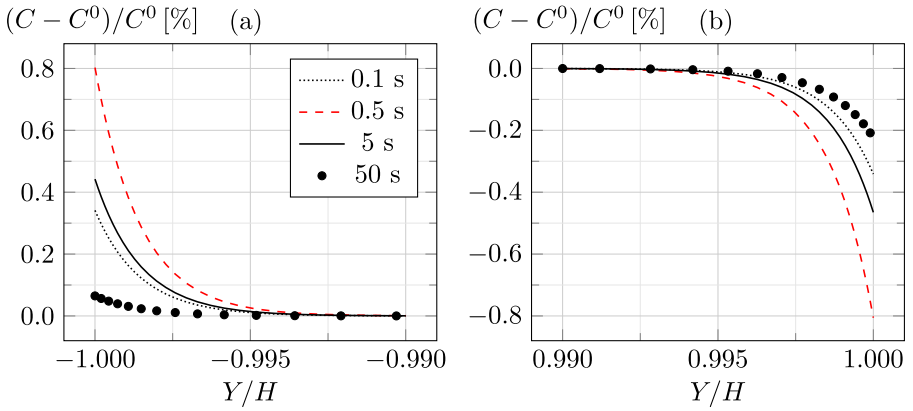

Fig. 18. Sensing: relative counterion concentration $[C(Y) - C^0]/C^0$ at $X = L/100$ in the cathode (a) and anode (b) boundary layers. The curves corresponding to the time instant ($\approx$ 0.5 s) at which counterions begin counter-diffusing are highlighted in red. (For interpretation of the references to color in this figure legend, the reader is referred to the web version of this article.)

Eq. (31). As the load is progressively applied, the IPMC bends toward the anode, with a tip displacement $u_Y^{\rm i} \approx 0.945\, u_Y^{\rm EB}$ at $t^{\rm i}$. As long as the load is maintained, the tip displacement increases with time, reaching the steady state value $u_Y^{\rm ss} \approx 0.985\, u_Y^{\rm EB}$. Therefore, the time-delayed displacement is $u_Y^{\rm ss} - u_Y^{\rm i} \approx 4\%\, u_Y^{\rm ss}$.

The observed poromechanics can be explained by temporarily resorting to small strains within the Euler–Bernoulli kinematics for the whole IPMC cross-section and disregarding the effect of the electric field. Under plane strain, the volume ratio reads $J(x,y) = 1 + \nu[\sigma_{xx}^{\rm mec}(x,y) + \sigma_{yy}^{\rm mec}(x,y)]/\lambda$. The applied load $\overline{T}$ is associated with a bending moment $M(x) = \overline{T}(x^2 - 2Lx + L^2)/2$, which is partly equilibrated by the total longitudinal stress in the membrane, such that $\sigma_{xx}^{\rm mec}(x,y) = p_{\rm s}(x,y) - [E/(1-\nu^2)]M(x)y/\beta$. Given the smallness of the applied load and the thinness of the IPMC, the equilibrium in the y direction requires that $\sigma_{yy}^{\rm mec}(x,y) \approx p_{\rm s}(x,y)$, as also confirmed by the finite element results. Consequently, the volume ratio can be rewritten as

$$J(x,y) \approx 1 + \frac{\nu}{\lambda}\left[2p_{\rm s}(x,y) - \frac{E}{1-\nu^2}\frac{M(x)}{\beta}y\right] = 1 + \frac{1}{2(\lambda+G)}\left[2p_{\rm s}(x,y) - \frac{4G(\lambda+G)}{\lambda+2G}\frac{M(x)}{\beta}y\right], \tag{32}$$

in which the last form is convenient to discuss the influence of λ. By neglecting $\partial p_{\rm s}/\partial x$, which is small compared to $\partial p_{\rm s}/\partial y$, the solvent mass balance (6) reduces to

$$\dot{p}_{\rm s}(x,y) - (\lambda+G)k_{\rm s}\frac{\partial^2 p_{\rm s}(x,y)}{\partial y^2} \approx \frac{4G(\lambda+G)}{\lambda+2G}\frac{\dot{M}(x)}{2\beta}y, \tag{33}$$

in which $k_{\rm s} = D_{\rm s}v_{\rm s}^2 C_{\rm s}^0/(RT)$. Eq. (33) is a diffusion-type equation to be solved, at each x, for the solvent pressure field $p_{\rm s}(y,t)$, given the initial condition $p_{\rm s}(y) = 0$ at $t = 0$ and the boundary conditions $\partial p_{\rm s}/\partial y\big|_{y=\pm H} = 0$, corresponding to imposing zero-flux at the electrodes. All the other relevant poromechanical fields can be readily reconstructed once Eq. (33) is solved.

While the load is linearly increased during the ramp of time length $t^{\rm i}$, the constant $\dot{M} = \overline{T}(x^2 - 2Lx + L^2)/(2t^{\rm i})$ generates a progressively increasing solvent pressure gradient along the membrane thickness. The solvent pressure $p_{\rm s}$ enters the equilibrium, such that $|\sigma_{xx}^{\rm mec}|$ is less than it would be for a non-porous material. Then, while the load is kept constant after the loading ramp, $\dot{M} = 0$ and the solvent progressively moves down its pressure gradient, $|p_{\rm s}|$ reduces, and a larger fraction of the applied load is equilibrated by $|\sigma_{xx}^{\rm mec}|$, which increases in time, while $|\sigma_{yy}^{\rm mec}| \approx |p_{\rm s}|$ decreases. Therefore, $|\mathcal{E}_{XX}|$ progressively increases, along with the IPMC deflection. At the steady state, the excess solvent pressure is dissipated, such that the solvent becomes irrelevant for the equilibrium. Correspondingly, in the membrane the total longitudinal stress σ_{xx} tends to coincide with its mechanical contribution $\sigma_{xx}^{\rm mec}$, and the deflection to the Euler–Bernoulli beam value $u_Y^{\rm EB}$.[6]

Within our framework, the smallness of the time-dependent deflection $u_Y^{\rm ss} - u_Y^{\rm i}$ (see Fig. 17) is explained by the fact that a considerable part of the applied load is instantaneously equilibrated by the longitudinal stress in the electrodes, $\sigma_{xx} \equiv \sigma_{xx}^{\rm mec} = -[E_{\rm e}/(1-\nu_{\rm e}^2)]My/\beta$.

So far, we have neglected the electric field contribution to the solvent flux. Actually, at the steady state, the solvent pressure is not exactly zero (see Fig. 14), as the component of the solvent flux proportional to $\nabla p_{\rm s}$ must balance the electro-osmotic contribution, proportional to $\mathbf{E}$. The mechanical stress state is in turn partly altered by the electro-osmotic flux of the solvent, but not by the Maxwell stress, which turns out to be negligible. Consequently, the final deflection is slightly less than that predicted by the Euler–Bernoulli beam theory (see Fig. 17).

[6] This picture is reminiscent of the consolidation problem of soil mechanics. However, in the classical problem of consolidation (Biot, 1941), the process is allowed by the drainage of water from the soil surface, whereby the total "vertical" stress is uniform along the soil depth. Here, differently, the solvent is prevented from draining, but the process is allowed by the presence of a total longitudinal stress gradient along the membrane thickness.

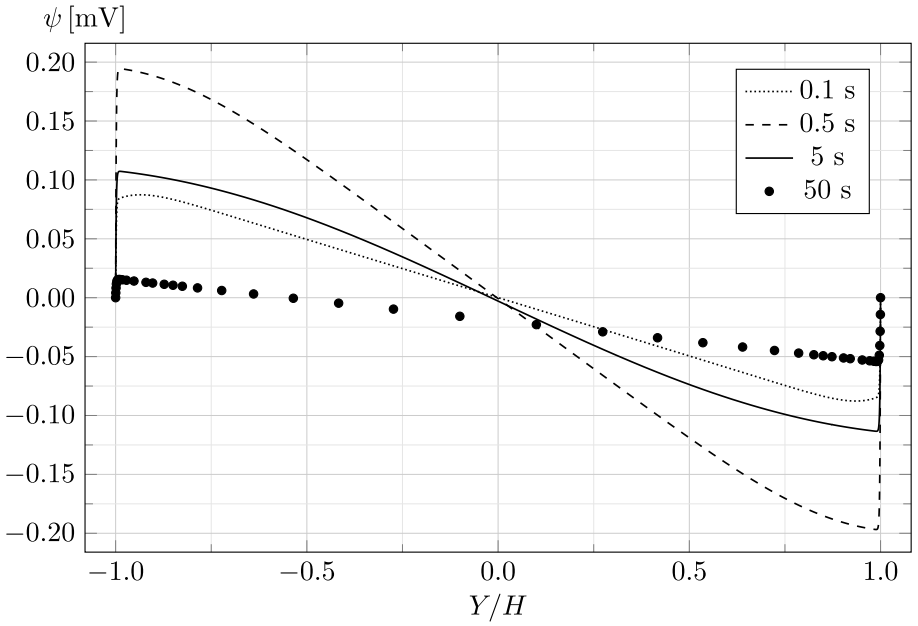

Fig. 19. Sensing: electric potential $\psi(Y)$ at $X = L/100$ in the membrane.

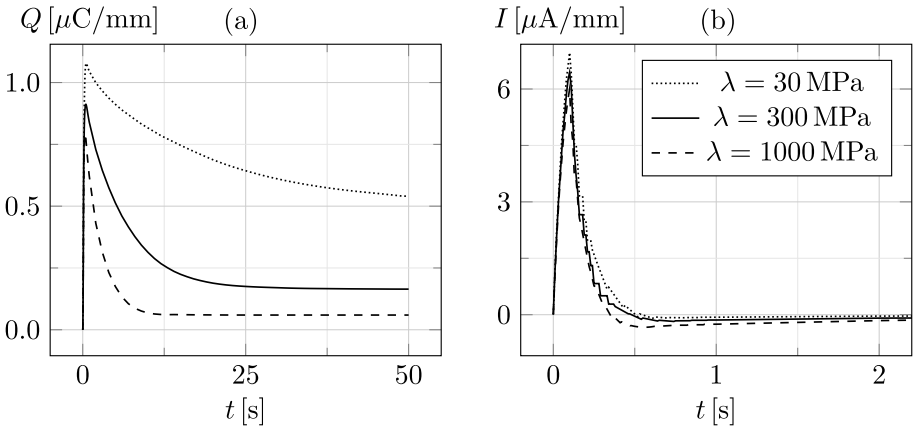

Fig. 20. Sensing: stored charge $Q(t)$ (a) and electric current $I(t)$ (b) per unit depth.

We can now comment on the electrochemical response elicited by the solvent flux, with reference to Fig. 18, in which we represent the counterion concentration $C(Y)$ in the boundary layers, and Fig. 19, where we display the electric potential $\psi(Y)$ in the membrane. At the cathode, C increases with time until $t \approx 0.5$ s, which is five times longer than the loading ramp duration t^{i}, and then decreases. The analogous opposite behavior is observed at the anode. We conclude that counterions are initially transported toward the cathode by convection with the solvent and by diffusion toward regions of larger volume ratio, until they counter-diffuse as their concentration gradient becomes sufficiently large. At the steady state, the convective and electrodiffusive fluxes are individually null. The electric potential field of Fig. 19 results from the counterion redistribution, on the basis of Gauss law (7).

In Fig. 20(a) we represent the time evolution of the stored charge per unit depth, defined as

$$Q = \int_0^L \left| D_Y(Y = \pm H) \right| \mathrm{d}X \, .$$

It increases until $t \approx 0.5$ s, when, with reference to the case $\lambda = 300\,\mathrm{MPa}$, it reaches the peak value $Q^{\mathrm{p}} \approx 0.91\,\mu\mathrm{C/mm}$. Then it starts decreasing slowly to the steady state value $Q^{\mathrm{ss}} \approx 0.16\,\mu\mathrm{C/mm} \approx 18\%\, Q^{\mathrm{p}}$. This decrease of Q, which can be deleterious for IPMCs employed in energy harvesting, is clearly due to the counterion counter-diffusion. The reversal of the counterion flux is also confirmed by the change in sign of the electric current per unit depth, defined as $I = \dot{Q}$, whose time evolution is shown in Fig. 20(b). The current increases with the load; then, it decreases rapidly and becomes negative at $t \approx 0.5$ s, when counterions begin

counter-diffusing; finally, it slowly goes to zero at the steady state. Qualitatively, the same results in terms of stored charge and electric current have been experimentally observed by Farinholt and Leo (2004) in response to an imposed tip displacement.

Fig. 20 also displays the time evolution of the stored charge and electric current obtained by varying the Lamé parameter λ, with G held equal to 50 MPa.[7] By decreasing λ, the peak stored charge Q^{p} increases and, most of all, the counterion counter-diffusion is milder, such that, for $\lambda = 30\,\mathrm{MPa}$, $Q^{\mathrm{ss}} \approx 0.5\,Q^{\mathrm{p}}$. This behavior is explained by the fact that, by diminishing λ, the solvent flux toward the cathode increases, along with the convective counterion flux. Indeed, Eq. (32) reveals that $|J(y)|$, and correspondingly $|C_{\mathrm{s}}(y)|$ through the constraint (3), increases by decreasing λ. Moreover, Fig. 20 shows that the discharge process requires a significantly larger time for smaller λ. This is explained by the diffusion equation (33), which shows that the "solvent pressure flux", defined as $-(\lambda+G)k_{\mathrm{s}}\partial p_{\mathrm{s}}/\partial y$, decreases with λ, thus requiring more time for the solvent pressure to be dissipated. This analysis might offer a criterion for selecting the most efficient ionomer for the IPMC membrane on the basis of the resulting elastic moduli.

Finally, we remark that, in sensing, the time-increasing asymmetry in $C(Y)$ and, especially, $\psi(Y)$ (see Figs. 18 and 19) can be captured only by considering a finite deformation framework. Indeed, although the deformations are relatively small (see Fig. 15), the time-varying deformation field non-negligibly modulates the electrochemistry, characterized in sensing by small deviations from the initial electroneutral state. This, of course, will be amplified by the application of larger loads than that considered here.

4. Concluding remarks

We have herein proposed a model for ionic polymer metal composites (IPMCs) by suitably modifying the electrochemomechanical theory of Cha and Porfiri (2014). As a main novelty, we have accounted for the transport of the solvent, which establishes the volumetric deformation of the membrane and cross-diffuses with the counterions.

Specifically, by referring to the mixture theory (Ateshian, 2007), we have regarded the IPMC membrane as the superposition of a solid phase, identifying with a negatively charged polymer, and a fluid phase, consisting of counterions immersed in a solvent. Toward the simplest possible model thoroughly describing the complex IPMC multiphysics, we have assumed that each constituent is incompressible and that the fluid phase is dilute, such that the volumetric deformation of the membrane only depends on the solvent redistribution. The model is governed by four coupled equations consisting of an overall momentum balance, the mass balances for solvent and counterions, and the Gauss law, to be solved for the displacement field, the solvent pressure, the counterion concentration, and the electric potential. We have proposed a free energy density encompassing the contributions due to the overall stretching of the membrane, the mixing of solvent and counterions, and the dielectric polarization of the membrane. As for the dissipation, we have accounted for cross-diffusion (Vanag and Epstein, 2009), that is, we have assumed that the (electro)chemical potential gradient of each species influences the flux of every species. Finally, we have modeled the electrodes as perfect electric conductors impermeable to the fluid phase, contributing to the overall bending stiffness of the IPMC.

Our model results in two mutually coupled building blocks, addressing the electrochemistry and the poromechanics of IPMCs. The electrochemistry is described by a Poisson–Nernst–Planck system of equations (Porfiri, 2008), augmented to consider the convective transport of counterions with the solvent, and modified, with respect to its conventional form, by being modulated through finite deformations. The poromechanics relies on Biot theory for saturated media (Biot, 1941), extended to include both the electro-osmotic transport of the solvent and the Maxwell stress. The electrochemistry drives the poromechanical response in actuation; dually, the poromechanics triggers the electrochemical response in sensing. This clearly emerges from the results of finite element analyses of the proposed theory implemented in the commercial code *COMSOL Multiphysics*®.

More specifically, in actuation the applied voltage drop across the electrodes elicits the migration of counterions toward the cathode; simultaneously, the electro-osmosis of the solvent in the same direction occurs, such that the cathode side swells, while the anode side shrinks. As soon as the solvent pressure gradient increases sufficiently, the solvent starts counter-diffusing, with a consequent relaxation of the bending deformation. Moreover, as the imbalance of ions near the electrodes grows asymmetrically in time (Porfiri et al., 2017), the Maxwell stress is responsible of a time-increasing bending deformation toward the cathode, which can overcome the effect of the solvent pressure, thus determining a reversal of the curvature (Asaka et al., 1995).

In sensing, the applied mechanical load establishes a solvent pressure gradient along the membrane thickness, which is then progressively dissipated as the solvent diffuses toward the cathode. Correspondingly, counterions move in the same direction by convection with the solvent and diffusion toward regions of larger volume ratio, and electrical charge is stored at the electrodes. When the counterion concentration gradient becomes large enough, counterions start counter-diffusing, with a consequent reduction of the harvested electrical energy, as experimentally observed in Farinholt and Leo (2004).

As a further novelty with respect to IPMC literature, we have described the membrane deformation through a compressible coupled hyperelastic model dependent on both Lamé parameters (Simo and Pister, 1984). We have demonstrated that, for a given shear modulus, the calibration of the first Lamé parameter λ allows one to modulate the entity of the back-relaxation in actuation and of the electric discharge in sensing, whereby larger values of λ emphasize both phenomena. On the one hand, this sheds light on the electrochemo-poromechanics of IPMCs. On the other hand, given the recent advancements in IPMC manufacturing (Carrico et al., 2015), it might provide a criterion for designing and selecting the optimal material for the membrane.

Future work should, first of all, focus on efficiently solving meaningful benchmarks governed by the here developed theory in order to quantitatively compare its predictions against *ad hoc* experimental results. In fact, our present finite element implementation

[7] Differently from the actuation problem, our numerical model exhibits convergence issues if we set $\lambda = 3000\,\mathrm{MPa}$ in this sensing problem, such that we limit λ to 1000 MPa.

in *COMSOL Multiphysics*® is computationally cumbersome and suffers convergence issues if we apply too large loads or set quite extreme values of some parameters, such as the first Lamé constant. Two strategies could be followed to address this issue: developing either an *ad hoc* finite element code or manageable and reliable semi-analytical solutions. Similar tasks have been recently accomplished for the Cha and Porfiri (2014) theory, encompassing a two-dimensional user defined finite element for continuum analysis (Boldini and Porfiri, 2020; Boldini et al., 2020) and enriched structural theories accounting for the through-the-thickness deformation of the membrane and for the IPMC laminate structure, combined with asymptotic methods for the electrochemistry (Leronni and Bardella, 2019; Boldini and Porfiri, 2020; Boldini et al., 2020).

Moreover, in order to accurately predict the experimental data, the model should be extended to account for the large variation of material properties due to both the electrode roughness (Porfiri, 2009) and the presence of metal particles in thin membrane regions adjacent to the electrodes, in the literature variously referred to as "intermediate layers" (Tiwari and Kim, 2010), "composite layers" (Cha et al., 2012), and "polymer-metal composite electrodes" (Liu et al., 2019). Accounting for these composite layers, possibly along with the volume occupied by counterions, would mitigate the large gradients of counterion concentration in the boundary layers and the associated high stress concentrations, at the price of additional computational difficulties (Porfiri et al., 2018; Volpini and Bardella, 2021). One would achieve an even more pronounced mitigation if such regions of variable properties were more appropriately modeled as functionally graded materials. Finally, this goal could be reached also by adopting a constitutive law limiting the maximum mechanical stress, for instance involving viscoplastic deformation (Silberstein and Boyce, 2010); in fact, such limitation, by equilibrium, would hamper a too large increase of Maxwell stress and solvent pressure, which are proportional to the fluid phase concentration gradient.

Establishing the range of applicability of the present theory would pave the way to elaborate on the main hypotheses the theory relies on. For instance, as a major point, removing the assumption of dilute fluid phase of solvent and counterions might quantitatively impact the predicted response, as IPMC electrochemistry is characterized by a large accumulation of counterions at the cathode. Let us recall that in Cha and Porfiri (2014) theory this effect is prevented by introducing a so-called steric coefficient in the Borukhov-like mixing free energy density of counterions and polymer chains (Borukhov et al., 2000). Within our framework, removing the dilute solution approximation would require adopting a proper mixing free energy density for a non-ideal solution, modifying the solvent and counterion fluxes to account for the friction between counterions and polymer network, and relating the volume ratio to both solvent and counterion concentrations. Finally, let us observe that, to the best of our knowledge, the mixing of solvent molecules and polymer chains has so far been overlooked in IPMC theories. Again, *ad hoc* experiments should demonstrate the need for such an addition to the modeling, which is instead a common feature in the literature of polyelectrolyte gels (Hong et al., 2010; Zhang et al., 2020).

CRediT authorship contribution statement

Alessandro Leronni: Conceptualization, Formal analysis, Software, Writing - original draft, Writing - review & editing. **Lorenzo Bardella:** Conceptualization, Supervision, Writing - original draft, Writing - review & editing.

Declaration of competing interest

The authors declare that they have no known competing financial interests or personal relationships that could have appeared to influence the work reported in this paper.

Acknowledgments

Work done within a research project financed by the Italian Ministry of Education, University, and Research (MIUR). The finite element *COMSOL Multiphysics*® model has been run at the Applied Acoustics Lab - University of Brescia. Prof. Maurizio Porfiri is acknowledged for helpful discussions.

References

Asaka, K., Oguro, K., 2000. Bending of polyelectrolyte membrane platinum composites by electric stimuli: Part II. Response kinetics. J. Electroanal. Chem. 480, 186–198.

Asaka, K., Oguro, K., Nishimura, Y., Mizuhata, M., Takenaka, H., 1995. Bending of polyelectrolyte membrane-platinum composites by electric stimuli I. Response characteristics to various waveforms. Polym. J. 27, 436–440.

Ateshian, G.A., 2007. On the theory of reactive mixtures for modeling biological growth. Biomech. Model. Mechanobiol. 6, 423–445.

Bard, A.J., Faulkner, L.R., 2001. Electrochemical Methods: Fundamentals and Applications, second ed. John Wiley & Sons, New York, USA.

Biot, M.A., 1941. General theory of three-dimensional consolidation. J. Appl. Phys. 12, 155–164.

Bluhm, J., Serdas, S., Schröder, J., 2016. Theoretical framework of modeling of ionic EAPs within the Theory of Porous Media. Arch. Appl. Mech. 86, 3–19.

Boldini, A., Bardella, L., Porfiri, M., 2020. On structural theories for ionic polymer metal composites: balancing between accuracy and simplicity. J. Elasticity 141, 227–272.

Boldini, A., Porfiri, M., 2020. Multiaxial deformations of ionic polymer metal composites. Internat. J. Engrg. Sci. 149, 103227.

Borukhov, I., Andelman, D., Orland, H., 2000. Adsorption of large ions from an electrolyte solution: a modified Poisson-Boltzmann equation. Electrochim. Acta 46, 221–229.

Bowen, R.M., 1980. Incompressible porous media models by use of the theory of mixtures. Internat. J. Engrg. Sci. 18, 1129–1148.

Boyce, M.C., Arruda, E.M., 2000. Constitutive models of rubber elasticity: A review. Rubber Chem. Technol. 73, 504–523.

Branco, P.C., Dente, J., 2006. Derivation of a continuum model and its electric equivalent-circuit representation for ionic polymer–metal composite (IPMC) electromechanics. Smart Mater. Struct. 15 (378).
Carrico, J.D., Traeden, N.W., Aureli, M., Leang, K., 2015. Fused filament 3D printing of ionic polymer-metal composites (IPMCs). Smart Mater. Struct. 24, 125021.
Cha, Y., Aureli, M., Porfiri, M., 2012. A physics-based model of the electrical impedance of ionic polymer metal composites. J. Appl. Phys. 111, 124901.
Cha, Y., Porfiri, M., 2014. Mechanics and electrochemistry of ionic polymer metal composites. J. Mech. Phys. Solids 71, 156–178.
Chen, Z., Tan, X., Will, A., Ziel, C., 2007. A dynamic model for ionic polymer–metal composite sensors. Smart Mater. Struct. 16, 1477–1488.
Chester, S.A., Anand, L., 2010. A coupled theory of fluid permeation and large deformations for elastomeric materials. J. Mech. Phys. Solids 58, 1879–1906.
Coussy, O., 2004. Poromechanics. John Wiley & Sons, Chichester, England.
Del Bufalo, G., Placidi, L., Porfiri, M., 2008. A mixture theory framework for modeling the mechanical actuation of ionic polymer metal composites. Smart Mater. Struct. 17, 045010.
Dorfmann, A., Ogden, R.W., 2005. Nonlinear electroelasticity. Acta Mech. 174, 167–183.
Farinholt, K., Leo, D.J., 2004. Modeling of electromechanical charge sensing in ionic polymer transducers. Mech. Mater. 36, 421–433.
Flory, P.J., 1942. Thermodynamics of high polymer solutions. J. Chem. Phys. 10, 51–61.
Gurtin, M.E., Fried, E., Anand, L., 2010. The Mechanics and Thermodynamics of Continua. Cambridge University Press, Cambridge, England.
Holzapfel, G.A., 2000. Nonlinear Solid Mechanics: A Continuum Approach for Engineering. John Wiley & Sons, Chichester, England.
Hong, W., Zhao, X., Suo, Z., 2010. Large deformation and electrochemistry of polyelectrolyte gels. J. Mech. Phys. Solids 58, 558–577.
Hong, W., Zhao, X., Zhou, J., Suo, Z., 2008. A theory of coupled diffusion and large deformation in polymeric gels. J. Mech. Phys. Solids 56, 1779–1793.
Huggins, M.L., 1941. Solutions of long chain compounds. J. Chem. Phys. 9, 440.
Huyghe, J.M., Janssen, J., 1997. Quadriphasic mechanics of swelling incompressible porous media. Internat. J. Engrg. Sci. 35, 793–802.
Jo, C., Pugal, D., Oh, I.K., Kim, K.J., Asaka, K., 2013. Recent advances in ionic polymer-metal composite actuators and their modeling and applications. Prog. Polym. Sci. 38, 1037–1066.
Kim, K.J., Shahinpoor, M., 2003. Ionic polymer-metal composites: II. Manufacturing techniques. Smart Mater. Struct. 12, 65–79.
Krishna, R., Wesselingh, J., 1997. The Maxwell-Stefan approach to mass transfer. Chem. Eng. Sci. 52, 861–911.
Leichsenring, P., Serdas, S., Wallmersperger, T., Bluhm, J., Schröder, J., 2017. Electro-chemical aspects of IPMCs within the framework of the theory of porous media. Smart Mater. Struct. 26, 045004.
Leronni, A., Bardella, L., 2019. Influence of shear on sensing of ionic polymer metal composites. Eur. J. Mech. A 77, 103750.
Liu, H., Xiong, K., Wang, M., 2019. A gradient model for young's modulus and surface electrode resistance of ionic polymer–metal composite. Acta Mech. Solida Sin. 32, 754–766.
MacMinn, C.W., Dufresne, E.R., Wettlaufer, J.S., 2016. Large deformations of a soft porous material. Phys. Rev. Appl. 5, 044020.
Nardinocchi, P., Pezzulla, M., Placidi, L., 2011. Thermodynamically based multiphysic modeling of ionic polymer metal composites. J. Intell. Mater. Syst. Struct. 22, 1887–1897.
Nemat-Nasser, S., Li, J.Y., 2000. Electromechanical response of ionic polymer-metal composites. J. Appl. Phys. 87, 3321–3331.
Ogden, R.W., 1984. Non-Linear Elastic Deformations. Ellis Horwood, Chichester, England.
Onsager, L., 1931. Reciprocal relations in irreversible processes. I.. Phys. Rev. 37, 405.
Porfiri, M., 2008. Charge dynamics in ionic polymer metal composites. J. Appl. Phys. 104, 104915.
Porfiri, M., 2009. Influence of electrode surface roughness and steric effects on the nonlinear electromechanical behavior of ionic polymer metal composites. Phys. Rev. E 79, 041503.
Porfiri, M., Leronni, A., Bardella, L., 2017. An alternative explanation of back-relaxation in ionic polymer metal composites. Extreme Mech. Lett. 13, 78–83.
Porfiri, M., Sharghi, H., Zhang, P., 2018. Modeling back-relaxation in ionic polymer metal composites: The role of steric effects and composite layers. J. Appl. Phys. 123, 014901.
Pugal, D., Jung, K., Aabloo, A., Kim, K.J., 2010. Ionic polymer-metal composite mechanoelectrical transduction: review and perspectives. Polym. Int. 59, 279–289.
Pugal, D., Kim, K.J., Aabloo, A., 2011. An explicit physics-based model of ionic polymer-metal composite actuators. J. Appl. Phys. 110, 084904.
Schicker, D., Wallmersperger, T., 2013. Modeling and simulation of the chemo-electro-mechanical behavior of ionic polymer-metal composites. J. Appl. Phys. 114, 163709.
Shahinpoor, M., Kim, K.J., 2001. Ionic polymer-metal composites: I. Fundamentals. Smart Mater. Struct. 10, 819–833.
Shahinpoor, M., Kim, K.J., 2004. Ionic polymer-metal composites: III. Modeling and simulation as biomimetic sensors, actuators, transducers and artificial muscles. Smart Mater. Struct. 13, 1362–1388.
Shahinpoor, M., Kim, K.J., 2005. Ionic polymer-metal composites: IV. Industrial and medical applications. Smart Mater. Struct. 14, 197–214.
Silberstein, M.N., Boyce, M.C., 2010. Constitutive modeling of the rate, temperature, and hydration dependent deformation response of Nafion to monotonic and cyclic loading. J. Power Sources 195, 5692–5706.
Simo, J.C., Pister, K.S., 1984. Remarks on rate constitutive equations for finite deformation problems: computational implications. Comput. Methods Appl. Mech. Engrg. 46, 201–215.
Tiwari, R., Kim, K.J., 2010. Effect of metal diffusion on mechanoelectric property of ionic polymer-metal composite. Appl. Phys. Lett. 97, 244104.
Tixier, M., Pouget, J., 2020. Validation of a model for an ionic electro-active polymer in the static case. Smart Mater. Struct. 29, 085019.
Vanag, V.K., Epstein, I.R., 2009. Cross-diffusion and pattern formation in reaction–diffusion systems. Phys. Chem. Chem. Phys. 11, 897–912.
Volpini, V., Bardella, L., 2021. Asymptotic analysis of compression sensing in ionic polymer metal composites: the role of interphase regions with variable properties. Math. Eng. 3, 1–31.
Volpini, V., Bardella, L., Rodella, A., Cha, Y., Porfiri, M., 2017. Modelling compression sensing in ionic polymer metal composites. Smart Mater. Struct. 26, 035030.
Zhang, H., Dehghany, M., Hu, Y., 2020. Kinetics of Polyelectrolyte Gels. J. Appl. Mech. 87, 061010.
Zhu, Z., Asaka, K., Chang, L., Takagi, K., Chen, H., 2013. Multiphysics of ionic polymer-metal composite actuator. J. Appl. Phys. 114, 084902.
Zhu, Z., Chang, L., Horiuchi, T., Takagi, K., Aabloo, A., Asaka, K., 2016. Multi-physical model of cation and water transport in ionic polymer-metal composite sensors. J. Appl. Phys. 119, 124901.